Monthly Notices
of the
ROYAL ASTRONOMICAL SOCIETY

MNRAS **461,** 2461–2479 (2016)
Advance Access publication 2016 June 20

doi:10.1093/mnras/stw1482

Precise limits on cosmological variability of the fine-structure constant with zinc and chromium quasar absorption lines

Michael T. Murphy,[1]★ Adrian L. Malec[1] and J. Xavier Prochaska[2]

[1]*Centre for Astrophysics and Supercomputing, Swinburne University of Technology, Hawthorn, VIC 3122, Australia*
[2]*Department of Astronomy and Astrophysics, UCO/Lick Observatory, University of California, 1156 High Street, Santa Cruz, CA 95064, USA*

Accepted 2016 June 16. Received 2016 June 16; in original form 2016 May 26

ABSTRACT

The strongest transitions of Zn and Cr II are the most sensitive to relative variations in the fine-structure constant ($\Delta\alpha/\alpha$) among the transitions commonly observed in quasar absorption spectra. They also lie within just 40 Å of each other (rest frame), so they are resistant to the main systematic error affecting most previous measurements of $\Delta\alpha/\alpha$: long-range distortions of the wavelength calibration. While Zn and Cr II absorption is normally very weak in quasar spectra, we obtained high signal-to-noise, high-resolution echelle spectra from the Keck and Very Large Telescopes of nine rare systems where it is strong enough to constrain $\Delta\alpha/\alpha$ from these species alone. These provide 12 independent measurements (three quasars were observed with both telescopes) at redshifts 1.0–2.4, 11 of which pass stringent reliability criteria. These 11 are all consistent with $\Delta\alpha/\alpha = 0$ within their individual uncertainties of 3.5–13 parts per million (ppm), with a weighted mean $\Delta\alpha/\alpha = 0.4 \pm 1.4_{\rm stat} \pm 0.9_{\rm sys}$ ppm (1σ statistical and systematic uncertainties), indicating no significant cosmological variations in α. This is the first statistical sample of absorbers that is resistant to long-range calibration distortions (at the <1 ppm level), with a precision comparable to previous large samples of $\sim$150 (distortion-affected) absorbers. Our systematic error budget is instead dominated by much shorter range distortions repeated across echelle orders of individual spectra.

Key words: line: profiles – instrumentation: spectrographs – dust, extinction – quasars: absorption lines – cosmology: miscellaneous – cosmology: observations.

1 INTRODUCTION

Quasar absorption spectra from 8–10-m optical telescopes have provided the most precise constraints on variations in the fine-structure constant, $\alpha \equiv e^2/\hbar c$, on cosmological scales. The high resolving power ($R \gtrsim 40\,000$) and high signal-to-noise ratio (S/N $\gtrsim$ 50 per resolution element) provided by echelle spectrographs on these telescopes allows the (usually) complex velocity structures of metal absorption lines to be resolved and compared between transitions via detailed profile fitting techniques. The introduction of the many-multiple (MM) method by Webb et al. (1999) and Dzuba, Flambaum & Webb (1999) enabled a further increase in precision: the detailed pattern of velocity shifts between many different metal transitions, caused by a possible variation in α, is fully utilized, providing additional sensitivity and increased statistics compared to previous analyses of alkali doublets (such as from C IV, Mg II, Si IV etc.; e.g. Bahcall, Sargent & Schmidt 1967; Wolfe, Brown & Roberts 1976; Cowie & Songaila 1995; Varshalovich, Panchuk & Ivanchik 1996; Murphy et al. 2001c). For each transition, i, analysed in a quasar absorption spectrum, its response to a relative α-variation, $\Delta\alpha/\alpha$, is characterized by its sensitivity coefficient, q_i, resulting in a velocity shift, Δv_i:

$$\Delta\alpha/\alpha \equiv \frac{\alpha_z - \alpha_0}{\alpha_0} \approx -\frac{1}{2}\frac{\Delta v_i}{c}\frac{\omega_i}{q_i} \equiv \frac{1}{2}\frac{\Delta v_i}{c}\frac{1}{Q_i}\,, \quad (1)$$

where ω_i is transition i's wavenumber. Therefore, together with the S/N of the spectrum and the sharpness of the absorption features, the spread in Q coefficients among the transitions analysed defines the precision with which $\Delta\alpha/\alpha$ can be measured.

Early MM studies focused on very large quasar absorber samples from archival spectra – those not observed or calibrated specifically for measuring $\Delta\alpha/\alpha$ – and maximized precision by comparing as many strong transitions as possible in each absorber. Interestingly, spectra from the Keck telescope's High Resolution Echelle Spectrometer (HIRES) indicated some evidence for a smaller α at redshifts $z_{\rm abs} = 0.2$–4.2 than the current laboratory value (Webb et al. 1999; Murphy et al. 2001a), with the final sample of 143 absorbers indicating $\Delta\alpha/\alpha = -5.7 \pm 1.1$ parts per million (ppm; Murphy, Webb & Flambaum 2003; Murphy et al. 2004). Spectra from the Very Large Telescope's (VLT's) Ultraviolet and Visual Echelle Spectrograph (UVES) did not replicate this result (Chand

★ E-mail: mmurphy@swin.edu.au

et al. 2004, though see Murphy, Webb & Flambaum 2008; Wilczynska et al. 2015), with the most recent large sample of 153 absorbers indicating $\Delta\alpha/\alpha = +2.1 \pm 1.2$ ppm (King et al. 2012). Nevertheless, when combined, the large HIRES and UVES samples supported self-consistent, 4σ evidence for a coherent, dipole-like variation in α across the sky (Webb et al. 2011; King et al. 2012). Studies of specific astrophysical or instrumental systematic effects could not explain these surprising results (e.g. Murphy et al. 2001b, 2003; King et al. 2012). Several detailed studies of very high S/N spectra of individual quasars have also reported $\Delta\alpha/\alpha$ measurements with $\gtrsim$3 ppm uncertainties (e.g. Quast, Reimers & Levshakov 2004; Levshakov et al. 2005, 2007; Molaro et al. 2008a; Murphy, Webb & Flambaum 2008; Agafonova et al. 2011; Molaro et al. 2013; Songaila & Cowie 2014) which were consistent with no α-variation but which did not rule out the large-sample results.

The most important systematic effects in this context are those that can distort the wavelength scale, inducing spurious velocity shifts *between* transitions at different wavelengths (cf. the same shift in all transitions; see equation 1). Given the surprising results above, such distortions from instrumental effects are of paramount concern. Empirical tests that are sensitive to all such effects, whether from known or, most importantly, unknown causes are therefore extremely valuable. Particularly successful has been the comparison of the relative wavelength scales established using the standard thorium–argon (ThAr) lamp technique, which was used in the quasar absorption studies, with a more accurate one embedded in the spectrum of the object itself. Molaro et al. (2008b) first compared the centroid wavelengths of discrete lines in solar atlases with those measured in ThAr-calibrated asteroid spectra from UVES, finding no long-range distortions of the ThAr wavelength scale. Similarly, Griest et al. (2010) and Whitmore, Murphy & Griest (2010) observed quasars through an iodine gas cell with HIRES and UVES, respectively, and found no long-range distortions (though they did identify short-range distortions – see Section 4.2.2). These early 'super-calibration' studies therefore provided some confidence that the ThAr-calibrated wavelength scales in the previous quasar absorption studies were accurate enough for reliable constraints on $\Delta\alpha/\alpha$.

Unfortunately, the spectra used in these early super-calibration studies appear to have been exceptions to the rule. Rahmani et al. (2013) cross-correlated several UVES asteroid spectra, taken between 2006 and 2012, with more accurate solar spectra recorded with Fourier-transform spectrometers (FTSs), and found long-range distortions up to 0.7 m s^{-1} Å^{-1}, enough to cause $\sim$10 ppm systematic effects in $\Delta\alpha/\alpha$. Bagdonaite et al. (2014) found smaller, though still substantial, distortions with a similar analysis of asteroid and 'solar-twin' stellar spectra. Songaila & Cowie (2014) also identified evidence for distortions by using telluric features in several quasar spectra. Recently, Whitmore & Murphy (2015) super-calibrated HIRES and UVES with archival asteroid and solar-twin spectra observed over two decades, finding that 0.2 m s^{-1} Å^{-1} distortions are ubiquitous in these spectrographs. Furthermore, they found that these likely explain the non-zero $\Delta\alpha/\alpha$ results from the large UVES sample of Webb et al. (2011) and King et al. (2012), and at least partially explain the earlier HIRES results of Webb et al. (1999) and Murphy et al. (2004). Therefore, it is likely that all $\Delta\alpha/\alpha$ results derived from UVES or HIRES spectra before 2014 are substantially affected by systematic errors due to long-range distortions. Most of these spectra cannot be corrected retrospectively for lack of solar-like spectra observed on the same nights as the quasar exposures.

Evans et al. (2014) measured $\Delta\alpha/\alpha$ in three absorbers towards a single bright quasar using three different spectrographs: HIRES, UVES and the Subaru telescope's High Dispersion Spectrograph (HDS). By comparing these spectra with each other, and super-calibrating them with contemporaneous asteroid and stellar iodine-cell observations, they corrected them for long-range distortions and obtained a weighted mean $\Delta\alpha/\alpha$ of $-5.4 \pm 3.3_{\rm stat} \pm 1.5_{\rm sys}$ ppm at $z_{\rm abs} = 1.1$–1.8. This is the only distortion-corrected measurement of $\Delta\alpha/\alpha$ published so far (though see Section 5 for discussion of a new, even more precise measurement in a single absorber by Kotuš, Murphy & Carswell 2016). It is therefore vital to supplement this with a substantial number of new measurements which either avoid or remove the long-range distortions evident in all three slit-based spectrographs on 8–10-m telescopes mentioned above.

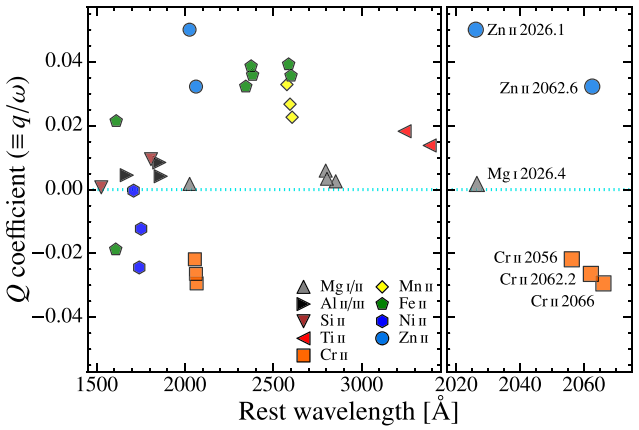

Figure 1. Left-hand panel: the sensitivity of transition frequencies to variation in α, represented by the Q coefficient, defined as $Q \equiv q/\omega$ (see equation 1), for transitions used in MM analyses to date. Right-hand panel: The small wavelength region in which the Zn/Cr II transitions that are the focus of this paper fall, showing their large Q values with opposing sign. The q values, laboratory wavelengths and other atomic data reviewed in Murphy & Berengut (2014) are used in throughout this work. The uncertainties in Q are $\sim$0.5 and 1.4×10^{-3} for the Zn and Cr II transitions, respectively, which are negligible for this work.

In this paper we seek to avoid the effects of long-range distortions by using only the closely spaced Zn II and Cr II transitions in an MM analysis. The principle behind this approach is evident in Fig. 1 which shows the Q coefficients of the transitions used in MM analyses to date, as reviewed in Murphy & Berengut (2014). The Zn II λλ2026/2062 doublet transitions have some of the largest *positive* Q coefficients, while the very nearby ($\Delta\lambda_{\rm rest} \leq 40$ Å) Cr II triplet transitions (λ2056, 2062, 2066) have amongst the largest *negative* Q values. That is, the Zn and Cr II transitions shift by large amounts, but in opposite directions if α varies, despite their very small wavelength separation. Therefore, analysing only the Zn/Cr II combination simultaneously provides high sensitivity to variations in α and low sensitivity to long-range distortions of the wavelength scale. Indeed, for an absorber at redshift $z_{\rm abs} = 1$, a typical 0.2 m s^{-1} Å^{-1} distortion would only cause a spurious $\approx$16 m s^{-1} shift between the *Zn* II λ2026 line and the Cr II triplet, corresponding to a systematic error in $\Delta\alpha/\alpha$ of just $\approx$0.3 ppm (via equation 1), substantially smaller than the statistical errors from the large HIRES and UVES samples or individual, high S/N absorbers. Note also that the *Zn* II λ2062 transition falls in between the *Cr* II λ2062 and λ2066 transitions, producing a more detailed, more characteristic pattern of velocity shifts due to a varying α. This increases resistance to long-range distortions as well as short-range distortions (see further discussion in Sections 4.2 and 5).

Here we obtain 12 independent MM measurements of $\Delta\alpha/\alpha$ with this Zn/Cr II approach, using both new and archival quasar spectra from HIRES and UVES. The observations and data reduction steps are described in Section 2, while Section 3 presents our approach to fitting the absorption profiles to measure $\Delta\alpha/\alpha$, and our analysis of each absorption system. The $\Delta\alpha/\alpha$ results and systematic errors are analysed in Section 4. The results are compared to others in the recent literature in Section 5, where we also compare the main advantages and disadvantages of the Zn/Cr II approach. Section 6 summarizes our conclusions.

2 QUASAR OBSERVATIONS AND DATA REDUCTION

2.1 Quasar selection

Our main aim is to obtain a precision in $\Delta\alpha/\alpha$ that is competitive with previous constraints, ∼2 ppm, from an ensemble of MM measurements using just the Zn/Cr II transitions. The statistical precision in $\Delta\alpha/\alpha$ available from an individual absorption system varies considerably according to several factors, particularly the S/N of the spectrum, and the optical depths and velocity structure of the metal absorption lines. Deeper absorption (though preferably unsaturated), with more distinct, narrow spectral features, provides more spectral information with which velocity shifts between transitions can be determined. However, the Zn and Cr II absorption in most absorption systems is very weak, presenting (rest-frame) Zn II equivalent widths of $W_{\rm r}(Zn\,{\rm II}\,\lambda2026) \lesssim 0.3$ Å. Even amongst the relatively high column-density damped Lyman α systems [i.e. those with $\log(N_{\rm H\,I}/{\rm cm}^{-2}) > 20.3$ cm^{-2}], 'metal-strong' systems that exceed this equivalent-width limit account for only ∼5 per cent of the population (Herbert-Fort et al. 2006). And, of course, even amongst these 'metal-strong' systems, few occur along lines of sight towards quasars bright enough to allow high-S/N echelle-resolution spectra to be easily obtained.

Therefore, to establish a sample of MM measurements with maximal statistical precision in $\Delta\alpha/\alpha$ and minimal additional telescope observing time, we selected targets for which existing UVES and/or HIRES spectra showed strong Zn and Cr II absorption lines, preferably with complex velocity structure with many distinct, narrow features. Weaker, less complex absorbers were included only when the quasar was significantly brighter, allowing a higher spectral S/N to be obtained so that a reasonably uniform precision on $\Delta\alpha/\alpha$ per absorber could be expected. We identified the nine quasars that are listed in Table 1, each with one absorber along its line of sight, that satisfied these criteria. The quasars have magnitudes ranging from $r = 16.1$–18.3 mag, emission redshifts $z_{\rm em} = 1.4$–2.7 and the absorbers fall in the redshift range $z_{\rm abs} = 1.0$–2.4.

2.2 Observations

Table 1 lists the observational details for the nine quasars and absorbers selected for this work. The spectra originate from both Keck/HIRES (Vogt et al. 1994) and VLT/UVES (Dekker et al. 2000), and three quasars have spectra from both telescopes/spectrographs; we analyse the HIRES and UVES spectra separately in these cases. Therefore, our final sample effectively comprises nine absorbers with 12 independent $\Delta\alpha/\alpha$ measurements.

The observations in Table 1 include ≈63 h of new observations specifically for this work and ≈38 h of archival exposures. Of the 54 h of HIRES exposures in total, 48 h (90 per cent) are new observations, with only Q1755+57 having a (6 h) contribution from archival spectra. For UVES, 70 per cent (32 h) of the 47 h of exposures are archival, while most UVES exposures of J0058+0041, J0226−2857 and J0841+0312 are new. For all quasars, multiple exposures were observed over several nights, split across several observing runs in most cases. Both the faintest quasar in our sample, Q1755+57, and also Q2206−1958 with its well-studied damped Lyman α system at $z_{\rm abs} = 1.921$, have the most exposures (13), while our UVES observations of the brightest target, J0841+0312, comprise the fewest (4). The sky transparency and seeing conditions varied considerably throughout the many different observing runs/nights. The seeing full-width-at-half-maximum (FWHM) was rarely less than 0.7 arcsec. The slit width used for all except one HIRES exposure was 0.86 arcsec, corresponding to a nominal resolving power of $R \approx 50\,000$ (obtained from the ThAr lamp exposures). For UVES, a larger variety of slit-widths was employed, but for all but three exposures a 0.8–1.0 arcsec slit was used, corresponding to (ThAr-based) nominal resolving powers $R = 42\,000$ down to 39 000, respectively. New observations were conducted in 'grey' lunations, except for the brightest three quasars (J0058+0041, PHL957 and J0841+0312) where bright lunations were also used.

During new observations in visitor mode[1] careful attention was paid to keeping the quasar centred within the slit by small adjustments to the telescope tracking. This was especially the case when only 'slit guiding' was possible in the absence of a nearby guide-star (mostly for HIRES), but this approach was also followed when 'offset guiding' from a nearby star was possible (mostly for UVES). A difference in quasar–slit alignment between two exposures of the same quasar will manifest itself as a velocity shift between corresponding absorption features in the two exposures. Indeed, HIRES observations by Evans et al. (2014) of a very bright quasar, for which these 'slit shifts' can be measured accurately, show that they are typically ≈200 m s^{-1}, corresponding to alignment differences between exposures of ≈4 per cent of the slit width. However, their observations of the same quasar with VLT/UVES and Subaru/HDS included small telescope tracking adjustments and this reduced the typical slit shift down to ≈100 m s^{-1}. The slit shift will, to a good approximation, be the same at all wavelengths, so no substantial distortion is introduced that would lead to systematic errors in $\Delta\alpha/\alpha$ (see equation 1).

However, a complicating factor arises when exposures which were taken in different spectrograph settings are combined. A 'setting shift' arises due to a difference between the average slit shifts for the exposures in two different settings. In the combined spectrum, the average slit shift then effectively varies with wavelength, i.e. setting shifts can create a distortion that may cause a systematic error in $\Delta\alpha/\alpha$. However, by minimizing the slit shifts in our new observations, we also minimize the setting shifts. Table 1 also shows that we restricted all our new observations (except for J0226−2857) to a single wavelength setting for each quasar. However, even for the quasars with multiple settings (mostly those with contributions from archival spectra) the effect of setting shifts is negated by our Zn/Cr II approach to measuring $\Delta\alpha/\alpha$: the Zn and Cr II transitions lie so close together that, in all except one of our spectra, they are all covered by the same exposures. Therefore, the effect of slit and setting shifts in our $\Delta\alpha/\alpha$ measurements is effectively avoided. The

[1] 'Visitor-mode' observations were conducted by the authors in person, whereas 'service-mode' observations were conducted entirely by observatory staff.

Table 1. Observational details of the quasar sample. The first column is the quasar name, where H or U superscripts denote Keck/HIRES or VLT/UVES observations, respectively, with the J2000 right-ascension and declination, and the quasar emission (z_{em}) and absorption (z_{abs}) redshifts provided. The spectrograph wavelength setting is specified as the approximate wavelength range for HIRES and the setting name (according to approximate central wavelength) for UVES. Total exposure times are specified for groups of exposures (specified in parentheses) in the same setting on each row; HIRES exposures of a given quasar were usually taken in the same setting, whereas a range of settings was often employed with UVES. The slit-widths correspond to the nominal resolving powers specified in the notes [a]. The final two columns give the total S/N per pixel, after all exposures are combined for each quasar, at rest-wavelengths (λ_{rest}) near the Cr II and *Mg* I λ2852 transitions. The on-chip binning for the UVES observations was 2×2, except for those of J0058+0041 where it was 1×1 (i.e. unbinned). All HIRES observations were binned only in the spatial direction (i.e. 2×1 binning). The dispersions of the combined spectra were set to 1.3 and 2.5 km s^{-1} for unbinned and binned spectra, respectively. Program identifiers, principle investigator surnames, observing mode (visitor or service) and dates are given in the notes for each observing run. The red cross-disperser was used for all HIRES observations except those taken in runs I, J and K.

Quasar	RA [hr] (J2000)	Dec. [deg] (J2000)	z_{em}	z_{abs}	Setting [nm]	Exposure time [s]	Slit-width[a] [arcsec]	S/N pix^{-1} at $\lambda_{rest}\sim$ 2060 Å	2852 Å
J0058+0041^{H}	00:58:24.75	+00:41:13.6	1.92	1.072	379–829[b]	37200 (11 × 3300–3600)$^{C, E, F}$	0.86	50	68
J0058+0041^{U}					390+564	17300 (6 × 2886)^{L}	0.8	29	31
					470+760	12900 (4 × 3000–3600)^{S}	1.0		
PHL957^{H}	01:03:11.27	+13:16:17.7	2.68	2.309	424–869	31620 (11 × 1200–3600)^{A}	0.86[c]	74	–
PHL957^{U}					390+860	7200 (2 × 3600)^{O}	1.0+0.9[d]	95	–
					390+590	15400 (3 × 5000–5400)^{Q}	0.9[e]		
J0108−0037^{U}	01:08:26.84	−00:37:24.2	1.37	1.371	390+580	14800 (4 × 3700)^{T}	1.0	48	58
					346+580	860 (2 × 430)^{V}	1.0		
					437+860	860 (2 × 430)^{V}	1.0		
J0226−2857^{U}	02:26:20.50	−28:57:50.8	2.17	1.023	390+564	12800 (4 × 2900–3300)^{M}	0.8	35	46
					390+580	9000 (3 × 3000)^{R}	1.2		
					437+760	13560 (4 × 2460–4200)^{M}	0.8		
J0841+0312^{H}	08:41:06.78	+03:12:06.6	1.94	1.342	414–848	26100 (9 × 2400–3600)$^{C, F}$	0.86	85	100
J0841+0312^{U}					470+760	11580 (4 × 2896)^{L}	0.8	41	72
J1029+1039^{H}	10:29:04.15	+10:39:01.6	1.79	1.622	435–869	21600 (6 × 3600)$^{C, D, F}$	0.86	36	29
J1237+0106^{H}	12:37:24.51	+01:06:15.4	2.02	1.305	400–848[f]	23600 (8 × 1600–3600)$^{C, D, F}$	0.86	30	36
Q1755+57^{H}	17:56:03.63	+57:48:48.0	2.11	1.971	435–869	31200 (9 × 3300–3600)$^{B, D}$	0.86	29	34
					318–605	23200 (4 × 4400–5400)$^{G, I, J, K}$	0.86		
Q2206−1958^{U}	22:08:52.07	−19:44:00.0	2.56	1.921	346+580	9000 (2 × 4500)^{P}	1.0	97	25
					390+564	20700 (6 × 2700–3600)^{N}	1.0		
					437+860	4200 (1 × 4200)^{N}	1.0		
					455+850	19600 (4 × 4200–5400)^{N}	0.9		

Notes. [a]The nominal resolving powers corresponding to the HIRES 0.86 and 1.15 arcsec slits are $R = 50000$ and 37000, respectively. For UVES, a 1.0 arcsec slit corresponds to a resolving power of $R = 42\,000$ and 39 000 in the blue and red arms, respectively, with proportionately higher (lower) R for narrower (wider) slits. [b]One 3300-s exposure was taken in the 336–810-nm setting. [c]A 1.15 arcsec slit was used for one 3300-s exposure due to poor seeing conditions. [d]1.0 arcsec for the blue arm, 0.9 arcsec for the red arm. [e]One 5400-s exposure was taken with a 1.0 arcsec slit. [f]One 1600-s exposure was taken in the 435–869-nm setting.

HIRES observing programs (all in visitor mode): [A]CS280Hr (Murphy): 2008 20–22 Aug. [B]CS280Hr (Murphy): 2008 07 Aug. [C]CS193Hr (Murphy): 2009 01 Feb. [D]W015Hr (Murphy): 2009 19 May. [E]W009Hr (Murphy): 2009 03 Nov. [F]G914Hr (Malec): 2009 29 Dec. [G]U11H (Prochaska): 2004 09 Sep. [I]U152Hb (Prochaska): 2006 02 Jun. [J]U157Hb (Prochaska): 2006 03 Jun. [K]U080Hb (Prochaska): 2006 18–19 Aug.

UVES observing programs: [L]084.A-0136 (Malec, service): 2009 12, 17 and 18 Oct for J0058+0041; 2009 15 and 27 Dec, 2010 09 Jan for J0841+0312. [M]084.A-0136 (Malec, visitor): 2009 8 and 9 Dec. [N]65.O-0158 (Pettini, visitor): 2000 29–31 May. [O]67.A-0022 (D'Odorico, service): 2001 16 and 17 Sep. [P]072.A-0346 (Ledoux, visitor): 2003 29 Oct. [Q]074.A-0201 (Srianand, visitor): 2004 8 and 9 Oct. [R]079.A-0600 (Bouché, service): 2007 25 and 28 Jul, 2007 5 Sep. [S]082.A-0682 (Dessauges-Zavadsky, visitor): 2008 05 May. [T]082.A-0569 (Srianand, service): 2008 21, 23 and 25 Nov, 2008 03 Dec. [V]083.A-0874 (Miniati, service): 2009 20 and 24 Aug.

exceptional case is Q1755+57, where the 318–605-nm wavelength setting, used in four exposures, covers only the *Zn* II λ2026 transition; the other nine exposures cover all the Zn and Cr II transitions. We discuss this exception in Section 3.2.8 and find that it is unlikely to have caused a significant systematic error. Note that, as discussed in Section 3.1, our profile fitting analysis does incorporate velocity structure information from the *Mg* I λ2852 transition which is often not covered by the same exposures as the Zn/Cr II lines. However, the velocity of that transition is de-coupled from the others in our fitting procedure so that setting shifts do not significantly affect our $\Delta\alpha/\alpha$ measurements (see Section 3.1 for details).

Establishing the wavelength scale of the quasar exposures is the most important calibration step for our $\Delta\alpha/\alpha$ measurements. Therefore, in all our new observations, a ThAr comparison lamp exposure was 'attached' to each quasar exposure, i.e. taken immediately after the quasar exposure without any changes to other spectrograph settings. We also restricted our selection of archival exposures to those that were either attached or, in some cases on UVES, taken immediately before the quasar exposure in the same setting. In the latter cases, the grating encoders will have been re-initialized between the ThAr and quasar exposure, potentially leading to velocity shifts between different exposures of the same quasar, though probably not substantial distortions; that is, this is effectively an additional slit shift that will, by the same argument as above, not strongly influence our $\Delta\alpha/\alpha$ measurements. Similarly, for two pairs of exposures for each of J0108−0037, Q1755+57 and Q2206−1958, the ThAr calibration exposure was attached to the later of the pair of quasar exposures. Again, this is unlikely to affect $\Delta\alpha/\alpha$ appreciably. Finally, for UVES archival spectra in the very red 760, 850 and 860-nm settings, the ThAr exposures were taken separately at the

end of the night. The only transition used in our analysis from these settings is $Mg\,\textsc{i}\,\lambda2852$ but, as described above, our fitting approach means that this will not affect the $\Delta\alpha/\alpha$ measurements.

2.3 Data reduction

All UVES exposures were reduced with the ESO Common Pipeline Language data-reduction software.[2] The general reduction scheme and the specific procedures used here were the same as those described in Bagdonaite et al. (2014), including the improvements to the ThAr line-fitting and selection (Murphy et al. 2007), and the extraction of the ThAr flux using the same spatial profiles weights as those established from the corresponding quasar exposure. As described by Malec et al. (2010), those same improvements were implemented within the HIREDUX[3] software suite which was used to reduce all the HIRES exposures. Additional improvements to the optimal extraction and blaze correction approach within HIREDUX are also documented by Malec (2016).

The extracted spectra were then processed and co-added using UVES_POPLER (Murphy 2016), code specifically written for optimally combining pipeline-reduced UVES and HIRES exposures. For UVES pipeline products, the pixel-space flux and 1σ error arrays from each echelle order, of each exposure, are redispersed on to a common log-linear wavelength scale after the wavelength solutions from the pipeline are converted to vacuum in the heliocentric reference frame. HIREDUX conducts these steps itself and we have checked that they are consistent with UVES_POPLER's implementation. UVES_POPLER scales the flux (and error) array in each echelle order to optimally match any orders overlapping with it and then combines the flux values from all exposures with inverse variance weighting in an iterative fashion to remove 'cosmic rays' and other artefacts. Any remaining artefacts were removed manually upon inspection of the absorption features of interest for this work. UVES_POPLER also automatically fits a low-order polynomial continuum which we inspected and adjusted with local, low-order corrections around absorption features.

For each quasar, all extracted exposures from all runs on a single spectrograph were initially combined to form a 'master spectrum', regardless of the differences in on-chip binning and spectral resolution (i.e. slit width) between observing runs. Combining all exposures allows for better artefact identification and a single continuum fit to the highest S/N representation of the spectrum. However, the contributing exposures were then grouped according to slit width and/or binning and saved as separate 'sub-spectra' of the master. These sub-spectra are analysed separately but simultaneously in our profile fitting approach, as described in Section 3.1.

We make the final master spectrum or sub-spectra used in the fit for each $\Delta\alpha/\alpha$ measurement publicly available in Murphy, Malec & Prochaska (2016).

3 ANALYSIS

3.1 Absorption profile fitting and $\Delta\alpha/\alpha$ measurement

The Zn/Cr II absorption profiles generally show a complex velocity structure and, for each system, these are fitted with multi-component Voigt profiles in order to derive the best-fitting $\Delta\alpha/\alpha$ which characterizes the pattern of any significant velocity shifts between the transitions. Our approach to fitting the absorption profiles is similar to many previous MM analyses (e.g. Murphy et al. 2001b, 2003; King et al. 2012; Molaro et al. 2013), and the same as that described in detail by Evans et al. (2014). It utilizes VPFIT version 9.5 (Carswell & Webb 2014) to minimize the χ^2 between a model of the absorption profile and the spectra. For a given absorber, the main steps and assumptions are as follows.

(i) $\Delta\alpha/\alpha$ is fixed to zero while a series of different models of the absorption profile is trialled, with successive models usually containing a larger number of fitted velocity components. The goal is to identify a single model that accounts for all the statistically significant structure in the observed profiles of the Zn and Cr II transitions simultaneously.

(ii) In all trial models, the redshifts (z) and Doppler b-parameters of corresponding Zn and Cr II components are tied together but their column densities, $N_{\rm Zn\,II}$ and $N_{\rm Cr\,II}$, are not linked. The b-parameters are limited to ≥1 km s^{-1} to avoid degeneracies with column densities in unresolved components and to ensure the χ^2 minimization converges reasonably quickly.

(iii) The preferred model is the one with the smallest χ^2 per degree of freedom, χ^2_ν. Other, similar criteria may be used to select the 'best' model (e.g. the Akaike information criterion, Akaike 1974; King et al. 2012), but the preferred model is usually either the same or very similar in these different approaches, so we use the simple χ^2_ν criterion here, as in Murphy et al. (2008).

(iv) $\Delta\alpha/\alpha$ is only introduced as an additional free parameter once the preferred model is finalized. This prevents $\Delta\alpha/\alpha$ from acquiring a spurious value during the process of establishing the preferred profile model. That process is also very interactive, so introducing $\Delta\alpha/\alpha$ as a free parameter only afterwards avoids any human bias. $\Delta\alpha/\alpha$ is then determined simultaneously with all the other free parameters (i.e. z, b, $N_{\rm Zn\,II}$ and $N_{\rm Cr\,II}$ for each component) via χ^2 minimization. The statistical uncertainty in $\Delta\alpha/\alpha$ is derived from the appropriate diagonal term of the final covariance matrix; degeneracies with other fitted parameters are negligible.

(v) We accept a fit, and the $\Delta\alpha/\alpha$ resulting from it, into our statistical analysis of the results (Section 4) only if three criteria are met by the preferred model: (i) $\chi^2_\nu < 1.2$; (ii) no long-range ($\gtrsim$5 pixel), significant and systematic excursions of the fit residuals in any transition; and (iii) no significant structure in the residuals common amongst the transitions, as judged from the 'composite residual spectrum' (CRS) (Malec et al. 2010) – the residuals from all transitions normalized by their error spectra, registered on the same velocity axis and averaged. These criteria guard against cases where low-level artefacts in the spectra, that cannot be attributed to Gaussian noise, may cause an appreciable systematic effect in $\Delta\alpha/\alpha$. These selection criteria were applied after determining $\Delta\alpha/\alpha$ to avoid rejecting fits in which poor residuals were caused by a real variation in α. However, in practice, we observe no large differences between the residuals before and after determining $\Delta\alpha/\alpha$ in any of the fits; none of the fits would have been rejected if the selection criteria were applied before $\Delta\alpha/\alpha$ was determined.

Physically, the assumption implicit in tying together the b-parameters of corresponding Zn and Cr II components is that turbulent broadening dominates over thermal broadening. The opposite choice could equally have been made. However, there is little practical difference between these assumptions for Zn and Cr because of

[2] http://www.eso.org/observing/dfo/quality/UVES/pipeline/pipe_reduc.html
[3] http://www.ucolick.org/~xavier/HIRedux

the small relative difference in their atomic masses (≈23 per cent; cf. ≈79 per cent for Mg and Fe). Furthermore, our aim is not to derive the physical properties of individual components (if that is even possible in most systems) but more practical: for determining $\Delta\alpha/\alpha$ it is sufficient to obtain a *physically plausible fit where all the statistically significant structure in a system's absorption profile is accounted for by the preferred model*. As discussed in Evans et al. (2014), this approach implies that, whatever broadening mechanism is assumed, the differences they cause in the model are effectively marginalized over in the χ^2 minimization process and will not affect $\Delta\alpha/\alpha$ significantly. The effect of different assumptions about the broadening mechanisms on $\Delta\alpha/\alpha$ has been explored by, e.g. Murphy et al. (2003), King et al. (2012) and Evans et al. (2014), and found to be unimportant. Therefore, we fit only turbulent velocity structures to our Zn and Cr II profiles.

A complication in fitting the Zn and Cr II simultaneously, and a difficulty when determining their (joint) velocity structure, is that the weak *Mg* I λ2026 transition falls just 50 km s^{-1} redwards of *Zn* II λ2026. In all but two of our absorbers (those towards J0108−0037 and PHL957), the profile structure extends over more than 50 km s^{-1} and, because these are strong metal absorbers, the *Mg* I λ2026 optical depth is sufficient to cause significant blending with parts of the *Zn* II λ2026 profiles. This blend must be modelled carefully if *Zn* II λ2026 is to contribute meaningful, unbiased constraints on $\Delta\alpha/\alpha$. Our approach is to fit the stronger – i.e. much better defined – *Mg* I λ2852 transition to strongly constrain the velocity structure of the *Mg* I λ2026 blend. However, we completely 'decouple' the Mg I fit from the Zn/Cr II fit in several ways: (i) the fitted Mg I velocity structure need not match that of the Zn/Cr II fit in the same absorber (though, of course, it will be similar); (ii) none of the Mg I component redshifts or *b*-parameters are tied to any Zn/Cr II components; and (iii) a velocity shift between the two Mg I transitions is fitted as an additional free parameter. This decoupling ensures that long-range systematic effects that generate spurious shifts between the *Mg* I λ2026 and 2852 transitions do not affect the $\Delta\alpha/\alpha$ parameter in the fit. We find the best-fitting velocity shifts to be typically ∼100–600 m s^{-1}, as expected for long-range distortions of the magnitude found in previous studies (i.e. $\lesssim$0.3 m s^{-1} Å^{-1}, e.g. Whitmore & Murphy 2015).

In cases where the master spectrum was split into two or more 'sub-spectra', with different resolutions (slit width) and/or dispersion (CCD binning), the sub-spectra were fitted simultaneously with the same absorption profile model. To allow for systematic shifts of sub-spectra in these different instrument and/or observing set-ups, an additional velocity shift between them was fitted as a free parameter. Again, this serves to decouple such systematics from the $\Delta\alpha/\alpha$ parameter in the fit. We find these shifts to have a magnitude $<$300 m s^{-1}, similar to the typical values found in other studies (e.g. Evans et al. 2014).

The laboratory wavelengths and oscillator strengths used for this analysis were reviewed in Murphy & Berengut (2014). These include isotopic structures calculated for the Cr II transitions (Berengut 2011) and *Zn* II λ2062 (Berengut, Dzuba & Flambaum 2003; Matsubara et al. 2003), the measured isotopic structure of *Zn* II λ2026 (Matsubara et al. 2003), the calculated hyperfine structure for the transitions of ^{67}Zn II (Campbell, Billowes & Grant 1997; Dixit et al. 2008), and the measured isotopic component wavelengths for *Mg* I λ2026 (Hannemann et al. 2006) and *Mg* I λ2852 (Salumbides et al. 2006). The laboratory wavelengths all have uncertainties $<$10 m s^{-1}; errors in these wavelengths should cause negligible systematic errors in $\Delta\alpha/\alpha$.

Table 2. Main result for each absorber. The quasar name, absorption redshift ($z_{\rm abs}$) and telescope (Tel.) identify the absorbers plotted in Figs 2–13. The best-fitting value of $\Delta\alpha/\alpha$ and its 1σ statistical uncertainty ($\sigma_{\rm stat}$) from the χ^2 minimization process are provided, along with the final χ^2 per degree of freedom, χ^2_ν. The systematic uncertainty estimate for each absorber ($\sigma_{\rm sys}$) is the quadrature sum of uncertainties from long-range distortions (0.3 ppm per absorber; Section 4.2.1), intra-order distortions (2.03 ppm per absorber; Section 4.2.2), and redispersion effects (0.49–2.28 ppm; Section 4.2.3). These results were derived using the terrestrial isotopic abundances for Zn and Cr; see discussion of this potential systematic error in Section 4.2.4. Note that the result from the VLT spectrum of J0058+0041, shown in italics, fails our selection criteria (Section 3.1) and is not considered in our statistical analysis in Section 4.3.

Quasar	$z_{\rm abs}$	Tel.	$\Delta\alpha/\alpha$ [ppm]	$\sigma_{\rm stat}$ [ppm]	$\sigma_{\rm sys}$ [ppm]	χ^2_ν
J0058+0041	1.072	Keck	−1.39	6.70	2.48	0.91
J0058+0041	*1.072*	*VLT*	*16.61*	*8.35*	*2.37*	*1.45*
PHL957	2.309	Keck	−1.44	6.47	2.26	0.99
PHL957	2.309	VLT	−1.94	12.89	2.70	1.06
J0108−0037	1.371	VLT	−3.96	2.74	2.11	1.07
J0226−2857	1.023	VLT	3.55	8.39	2.37	1.03
J0841+0312	1.342	Keck	2.98	2.99	2.13	0.77
J0841+0312	1.342	VLT	5.38	4.21	2.16	1.03
J1029+1039	1.622	Keck	−1.52	9.80	2.55	0.70
J1237+0106	1.305	Keck	−4.46	8.02	3.07	0.76
Q1755+57	1.971	Keck	4.68	4.15	2.16	0.86
Q2206−1958	1.921	VLT	−4.60	6.02	2.24	1.06

3.2 Fits to individual absorption systems

Below we discuss the fit to each absorption system, highlighting complexities or difficulties where relevant. The fitted parameters and their uncertainties are provided in electronic, VPFIT format in Murphy et al. (2016) for full transparency and reproducibility. Table 2 summarizes the main results from each fit, including the best-fitting value of $\Delta\alpha/\alpha$, its statistical uncertainty and χ^2_ν.

3.2.1 $z_{\rm abs} = 1.072$ towards J0058+0041

This absorber extends over 120 km s^{-1} in Zn/Cr II but has two main (i.e. stronger and better defined) spectral features at −30 and 0 km s^{-1}, as shown in Fig. 2 (the fit to the HIRES spectrum) and Fig. 3 (UVES). These contribute the main constraints on $\Delta\alpha/\alpha$. The blending *Mg* I λ2026 velocity structure extends over much of the *Zn* II λ2026 transition but, as explained in Section 3.1 above, *Mg* I λ2852 is used in both the HIRES and UVES spectra to model this blend (visually, this may be more easily appreciated by first referring to the simpler, narrower absorption towards J0108−0037 in Fig. 6). The HIRES and UVES profiles were fit separately, with similar but not identical models, providing independent $\Delta\alpha/\alpha$ measurements. The UVES spectrum comprised two sub-spectra, composed of the unbinned and 2×2-binned exposures, and these were fitted simultaneously as separate spectra (i.e. with the same absorption profile model) with a velocity shift between them as an additional free parameter, as described in Section 3.1. Visual inspection of Fig. 3 shows no evidence of substantial inconsistencies between the two differently binned spectra.

Two small differences between the HIRES and UVES models in Figs 2 and 3 are worth considering as examples.

(i) One velocity component, at −20 km s^{-1} in the HIRES model, is fitted at slightly lower velocity in the UVES model. The weak,

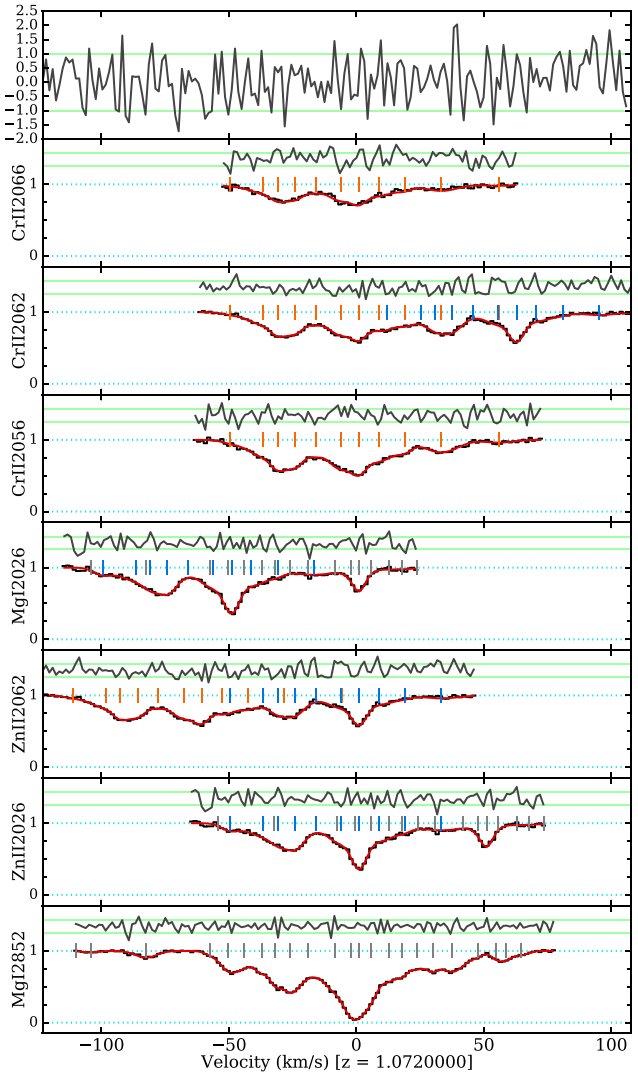

Figure 2. Fit to the Keck/HIRES spectrum of the $z_{\rm abs} = 1.072$ absorber towards J0058+0041. The lower seven panels each show the continuum-normalized flux versus velocity (relative to the redshift in brackets) for one of the Zn II, Cr II and/or Mg I transitions fitted to measure $\Delta\alpha/\alpha$. The normalized spectrum (black histogram) is overlaid by the fit (red solid line) which comprises Voigt profile components at the velocities marked by the ticks (short vertical lines; orange for Cr II, blue for Zn II and grey for Mg I). The residual spectrum, normalized by the 1σ error spectrum, is plotted (grey line) above the spectrum, with its $\pm1\sigma$ levels marked by the green solid lines. The top panel shows the composite residual spectrum (CRS; grey line) in units of standard deviations, relative to its $\pm1\sigma$ levels (green solid lines), derived by stacking the normalized residuals of all transitions shown. Note that the *Zn* II λ2062 and *Cr* II λ2062 transitions are blended with each other, as are *Zn* II λ2026 and *Mg* I λ2026; our approach to fitting these blends, using the *Mg* I λ2852 line, is discussed in Section 3.1.

broader absorption this component is responsible for means that it will have no significant effect on $\Delta\alpha/\alpha$;

(ii) The reddest component in Cr II is too weak to be fitted in Zn II. It is present in both the HIRES and UVES models but, given the S/N of the spectra, it was statistically unnecessary to fit in the Zn II transitions.

The effect of such weak, often broad velocity components on $\Delta\alpha/\alpha$ is negligible, so we omit discussion of similar cases in the rest of this section, focusing instead on components which, at first, may be suspected of having affected $\Delta\alpha/\alpha$ more significantly.

The fit to the HIRES spectrum in Fig. 2 shows no evidence of significant, many-pixel excursions in the residuals of any transition, nor in the composite residual spectrum (CRS), and the final $\chi^2_\nu = 0.91$. Therefore, the best-fitting $\Delta\alpha/\alpha$ value shown in Table 2, $-1.4 \pm 6.7_{\rm stat}$, is accepted for our main results.

By contrast, the fit to the UVES spectrum in Fig. 3 shows a run of significant residuals at -27 km s^{-1} in *Cr* II λ2056 in the unbinned spectrum, the CRS may have some significant structures, and Table 2 shows a $\chi^2_\nu = 1.45$. An extensive set of trial profile models was explored to remedy these problems, but even models with significantly more velocity components did not solve them. We therefore reject this system from our main results in Section 4. This is the only one of the 12 possible $\Delta\alpha/\alpha$ measurements that we reject in this way.

3.2.2 $z_{\rm abs} = 2.309$ towards PHL957

Figs 4 and 5 show our fits to the HIRES and UVES spectra of this absorber, which is relatively narrow, comprising two main spectral features spanning just ≈40 km s^{-1}. Therefore, there is no blending from *Mg* I λ2026 in these main features of *Zn* II λ2026. This is important because, at this redshift, the *Mg* I λ2852 is heavily blended with telluric absorption and so cannot be used to help constrain any *Mg* I λ2026 absorption. We detect very weak absorption at 30–70 km s^{-1} in the Cr II transitions. Much stronger transitions (e.g. *Al* II λ1670, *Si* II λ1526, *Fe* II λ2374 etc.) show another two spectral features at these velocities, so our fit includes two weak velocity components to account for them. However, we do not include those components in the Zn II fit because they are so weak, providing no significant constraints on $\Delta\alpha/\alpha$ and, in *Zn* II λ2026, they would be blended with any weak *Mg* I λ2026 absorption.

The fits to both the HIRES and UVES spectra in Figs 4 and 5 show no evidence of significant, many-pixel excursions in the residuals of any transition, nor in the CRSs, and the final χ^2_ν values in Table 2 satisfy our selection criterion in Section 3.1. Therefore, both results from this absorber are accepted in our main results.

3.2.3 $z_{\rm abs} = 1.371$ towards J0108−0037

Fig. 6 shows that the Zn and Cr II absorption in this system has a very similar structure to that in the absorber towards PHL957, with two main features spanning only ≈40 km s^{-1}. Three closely spaced components are required in the bluer spectral feature, with one component (the reddest of the three) being very narrow, just above our $b = 1.0$-km s^{-1} limit. A fit with only two components in this spectral feature has substantially poorer χ^2_ν so is rejected in preference to the three-component model. The lower redshift of this system allows *Mg* I λ2852 to be included, and Fig. 6 shows that no blending of *Mg* I λ2026 with *Zn* II λ2026 occurs. Indeed, as was necessary for PHL957, the Mg I fit could have been entirely neglected from this absorber and the fit to *Zn* II λ2026 simply truncated at ≈25 km s^{-1}. We retain these features here to demonstrate these points for PHL957, but they have no bearing on $\Delta\alpha/\alpha$. *Mg* I λ2852 also shows that a weak component exists in the red wing of the redder spectral feature, and we find that a similar component is required to fit the Cr II lines. However, this component is very weak, and is not required to fit the weaker Zn II transitions.

The fit to the UVES spectrum in Fig. 6 satisfies our selection criteria in Section 3.1, so is accepted in our main results.

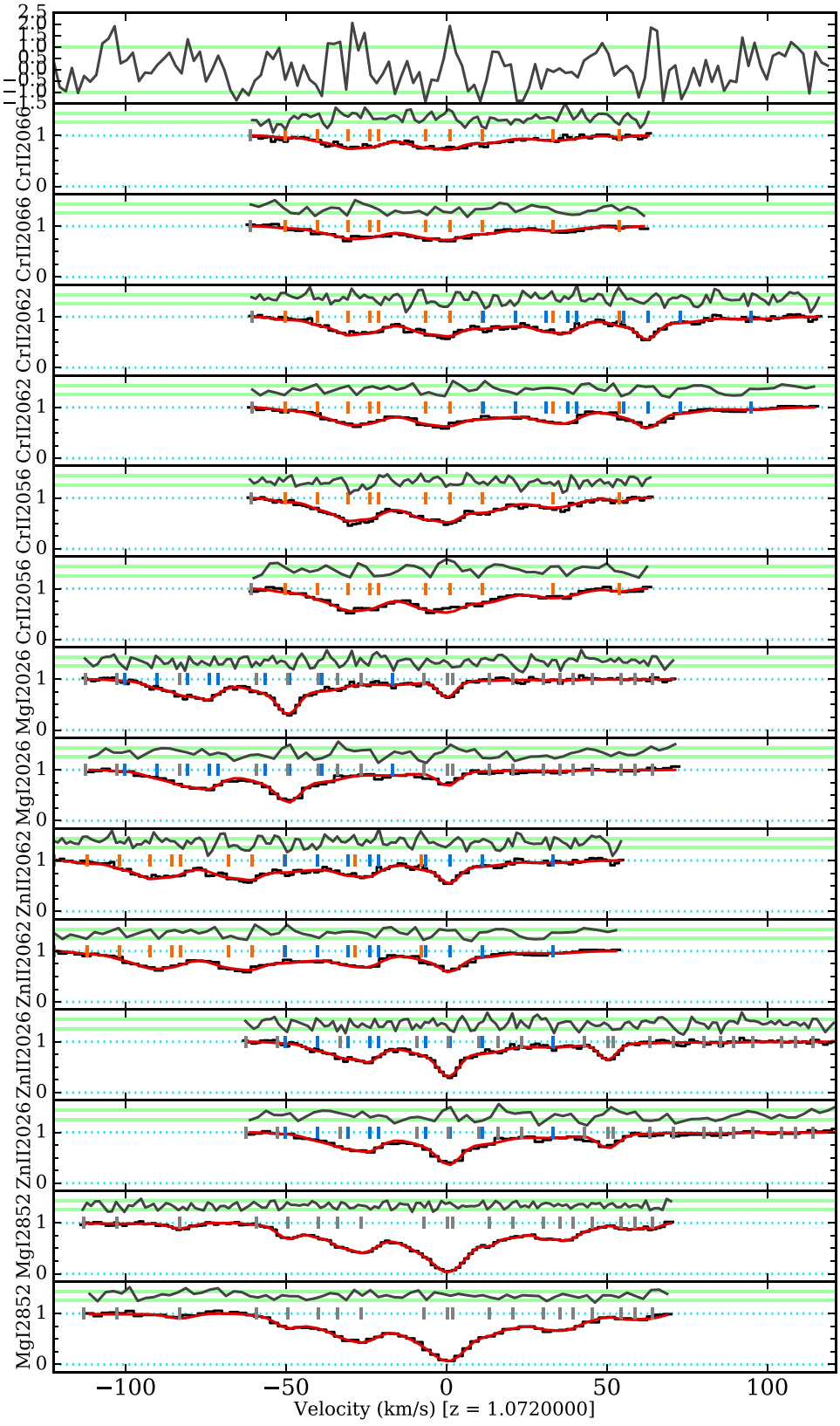

Figure 3. Same as Fig. 2 but for the VLT/UVES spectrum of the $z_{\rm abs} = 1.072$ absorber towards J0058+0041. Two sub-spectra are shown for each transition, one comprising unbinned exposures (upper panel for each transition) and another comprising 2×2-binned exposures (lower panel for each transition). Note that these data and the fit fails our selection criteria for inclusion in our main results (see text).

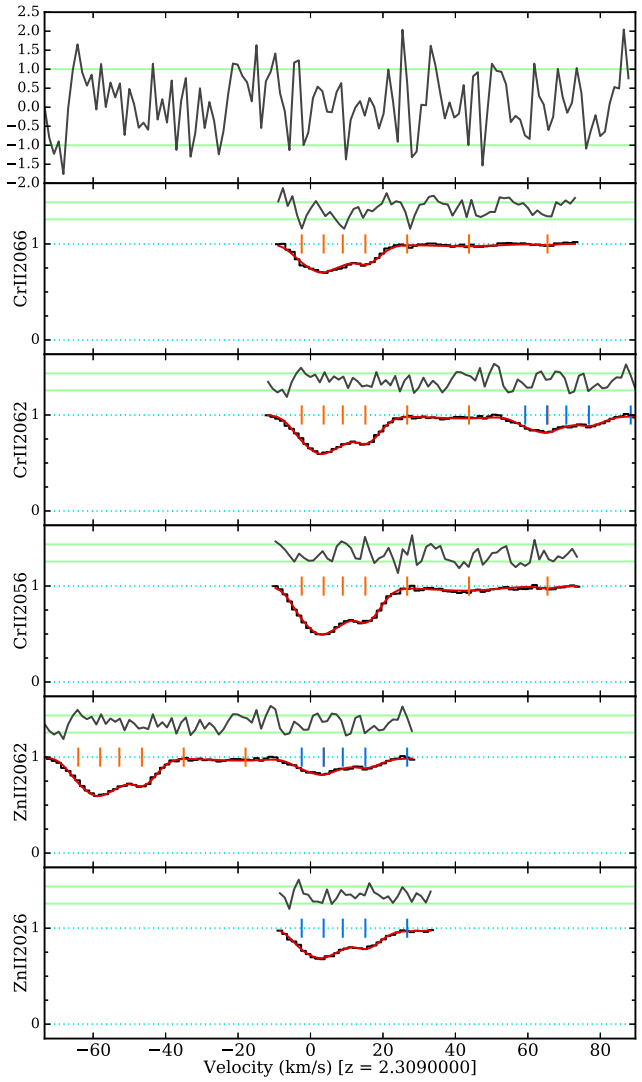

Figure 4. Same as Fig. 2 but for the Keck/HIRES spectrum of the $z_{\rm abs} = 2.039$ absorber towards PHL957. *Mg* I λ2852 is heavily blended with telluric absorption but is not required because the narrow absorption profile means *Mg* I λ2026 does not blend with *Zn* II λ2026.

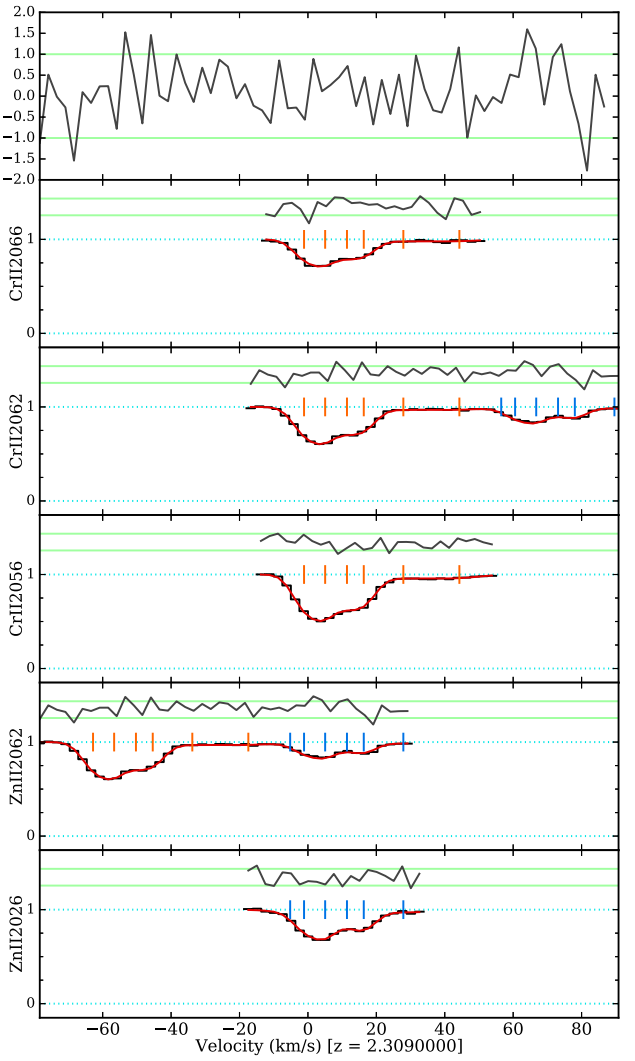

Figure 5. Same as Fig. 4 but for the VLT/UVES spectrum of the $z_{\rm abs} = 2.309$ absorber towards PHL957.

3.2.4 $z_{\rm abs} = 1.023$ towards J0226−2857

Two sub-spectra were created from the master UVES spectrum for analysis of this absorber, one from the four higher resolution, 0.8 arcsec slit-width exposures, the other from the three lower resolution, 1.2 arcsec slit-width exposures (see Table 1). All exposures had 2×2 on-chip CCD binning (native bin size is ≈2.3 km s^{-1}) so, to reduce information loss from redispersion when combining the exposures, we used two different dispersions, 2.0 and 2.5 km s^{-1}, for the higher and lower resolution sub-spectra, respectively.

Fig. 7 shows the separate, simultaneous fit to both sub-spectra, with a velocity shift between them fitted as an additional free parameter, as described in Section 3.1. The velocity structure is quite complex, spanning 180 km s^{-1} with three main, fairly separate spectral features in Zn and Cr II. The bluest two of these Zn/Cr II features must be fitted with 6–7 velocity components each. The most important part of the profile for constraining $\Delta\alpha/\alpha$ is the deepest, sharpest feature at 0 km s^{-1}, especially its sharp red wing. The other features, being smoother and shallower, constrain $\Delta\alpha/\alpha$ correspondingly less well. No substantial differences were required between the velocity structures fitted to the Zn and Cr II transitions. With such a broad velocity structure, blending with *Mg* I λ2026 is important for the *Zn* II λ2026 fit. For this purpose, the strong, very broad (380 km s^{-1} with ≈10 spectral features) profile of *Mg* I λ2852 was available in the higher resolution sub-spectrum at a high S/N.

Preliminary fits revealed that the lower resolution sub-spectrum contained two small (≈6-pixel) regions of significantly lower flux compared to the high-resolution sub-spectrum: in *Zn* II λ2062 at 25 km s^{-1} and in *Cr* II λ2066 at −30 km s^{-1}. We therefore truncated the blue and red edges of the fitting regions in these transitions, in the lower resolution sub-spectrum only, just above and below these velocities, respectively. Including these regions in our fiducial fit does not change $\Delta\alpha/\alpha$ significantly (it decreases by ≈0.6 ppm, less than a tenth of the statistical error in this absorber) but would disqualify this absorber from entering our statistical sample. Indeed, comparing sub-spectra in this way is an effective means of checking for artefacts that may otherwise cause systematic effects in individual systems.

The final fit to the two UVES sub-spectra in Fig. 7 shows no evidence of significant problems with the residuals in individual

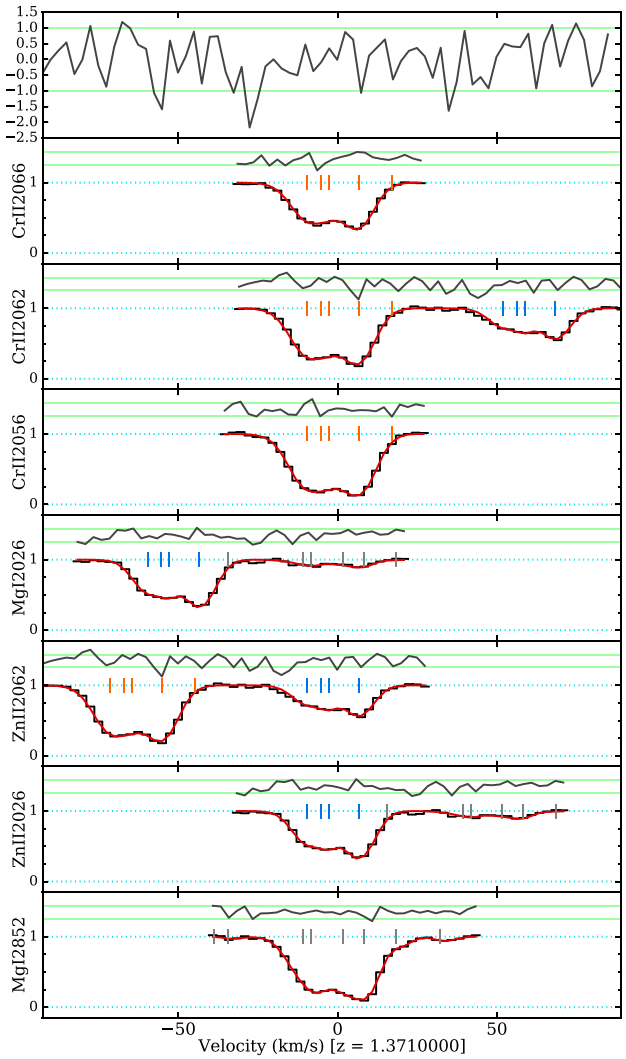

Figure 6. Same as Fig. 2 but for the VLT/UVES spectrum of the $z_{\rm abs} = 1.371$ absorber towards J0108−0037.

transitions or the CRS, and the final χ^2_ν in Table 2 satisfies our criterion in Section 3.1 for accepting this absorber into our main results.

3.2.5 $z_{\rm abs} = 1.342$ towards J0841+0312

Figs 8 and 9 show our fits to the HIRES and UVES spectra of this absorber. Zn/Cr II absorption is detected over 120 km s^{-1} in two spectral features, with the deepest one around 25 km s^{-1} constraining $\Delta\alpha/\alpha$ most strongly. The relative weakness of the spectral feature at −80 km s^{-1} means that the *Mg* I λ2026 blending with the main spectral feature of *Zn* II λ2026 is very weak (though not entirely negligible). There is additional absorption from a blend (from another redshift) in the blue spectral feature of *Cr* II λ2066, below ≈− 15 km s^{-1}, so this spectral feature is not included in the fit to that transition.

The fits to both the HIRES and UVES spectra in Figs 8 and 9 show no evidence problems in the residuals, nor in the CRSs, and the final χ^2_ν values in Table 2 satisfy our selection criterion in Section 3.1 for accepting both results for this absorber into our main results.

3.2.6 $z_{\rm abs} = 1.622$ towards J1029+1039

The Keck/HIRES spectrum of this absorber in Fig. 10 shows very complex and broad velocity structure, spanning 230 km s^{-1} in Zn/Cr II, dominated by one main spectral feature at −40 km s^{-1} comprising many velocity components. The overall shape of that feature is relatively broad and smooth, with few sharp sub-features, leading to a weaker constraint on $\Delta\alpha/\alpha$ than in most other absorbers studied here. No substantial differences were required between the velocity structures fitted to the Zn and Cr II transitions. With such a broad velocity structure, blending with *Mg* I λ2026 is important for the *Zn* II λ2026 fit; the high S/N of the *Mg* I λ2852 transition is more than adequate for this purpose. Fig. 10 shows no evidence of significant, many-pixel deviations in the residuals in individual transitions or the CRS, and the final χ^2_ν in Table 2 satisfies our criterion in Section 3.1 for accepting this absorber into our main results.

3.2.7 $z_{\rm abs} = 1.305$ towards J1237+0106

The Keck/HIRES spectrum of this absorber in Fig. 11 shows many similarities to that of J1029+1039 in Fig. 10, with very complex and broad velocity structure (spanning 215 km s^{-1} in Zn/Cr II). In this case the constraints on $\Delta\alpha/\alpha$ are dominated by two stronger, sharper spectral features, at −20 and 90 km s^{-1}, each comprising several velocity components. Despite the complexity, no substantial differences were required between the velocity structures fitted to the Zn and Cr II transitions. As with J1029+1039, the significant blending from *Mg* I λ2026 is strongly constrained with the high S/N spectrum of *Mg* I λ2852. There is no evidence for problems with the individual residual spectra or the CRS in Fig. 7, and the final χ^2_ν in Table 2 satisfies our criterion in Section 3.1. We therefore accepted this absorber into our main results.

3.2.8 $z_{\rm abs} = 1.971$ towards Q1755+57

This absorber is significantly more complex than any other in this study. The Keck/HIRES spectrum in Fig. 12 shows that the Zn/Cr II absorption spans 450 km s^{-1} (and *Mg* I λ2852 spans 540 km s^{-1}), with four prominent spectral features at −180, 10, 70 and 120 km s^{-1}, all of which comprise many velocity components. The sharpest features in both Zn and Cr II are those at 70 and 120 km s^{-1} and these provide the strongest constraints on $\Delta\alpha/\alpha$. It is interesting that the features at −180 and 10 km s^{-1} are strong and sharp in Zn II but much less so in Cr II; this is most likely due to enhanced levels of dust-depletion in these parts of the absorber (e.g. Pettini, Boksenberg & Hunstead 1990; Zych et al. 2009). The velocity structure comprises a total of 44 fitted velocity components in Cr II, with all but 3 of those required to fit the Zn II absorption. These three components sit in the extreme blue and red parts of the profile, at −189.5, 135.8 and 169.7 km s^{-1}, and are all very weak in Cr II, so their presence in, or absence from the fit to Zn II has no significant effect on $\Delta\alpha/\alpha$.

As with the other moderately complex absorbers in this study, towards J1029+1039 and J1237+0106, fitting the *Mg* I λ2026 that blends with *Zn* II λ2026 is very important but is also tightly constrained by the high S/N of the *Mg* I λ2852 transition. And, even though this absorber is very complex, and the Voigt profile fitting analysis correspondingly difficult and time-consuming, the final fit in Fig. 7 shows no evidence of significant runs of deviant residuals in individual transitions or the CRS. The final χ^2_ν in Table 2 is well

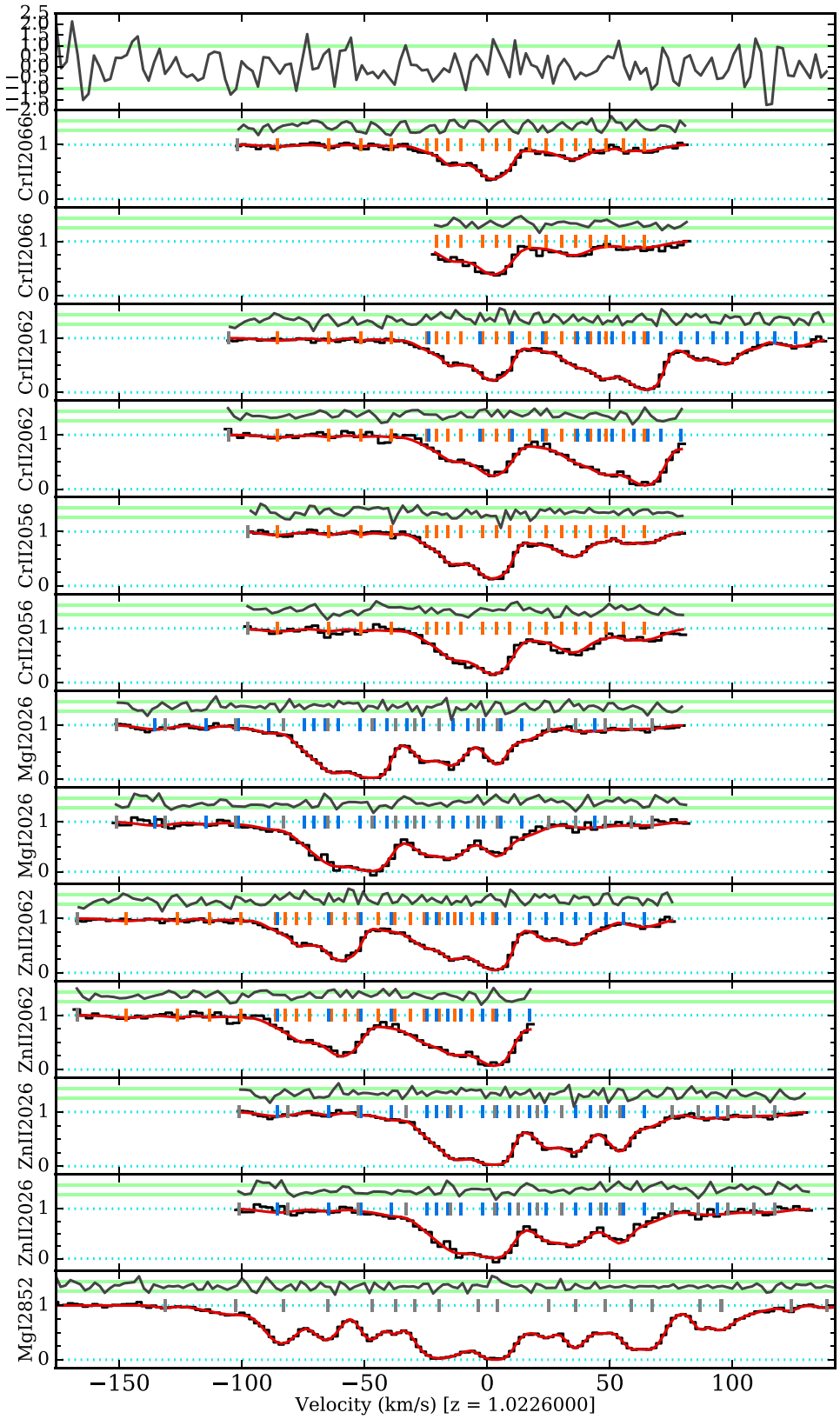

Figure 7. Same as Fig. 3 but for the VLT/UVES spectrum of the $z_{\rm abs} = 1.023$ absorber towards J0226−2857. Two sub-spectra are shown for each transition, one comprising higher resolution, 0.8 arcsec slit-width exposures with 2.0 km s^{-1} dispersion (upper panel for each transition) and another comprising lower resolution, 1.2 arcsec slit-width exposures with 2.5 km s^{-1} dispersion (lower panel for each transition). The *Mg* I λ2852 absorption continues at velocities >140 km s^{-1} but has no bearing on the blending of *Mg* I λ2026 with *Zn* II λ2026 and is not shown.

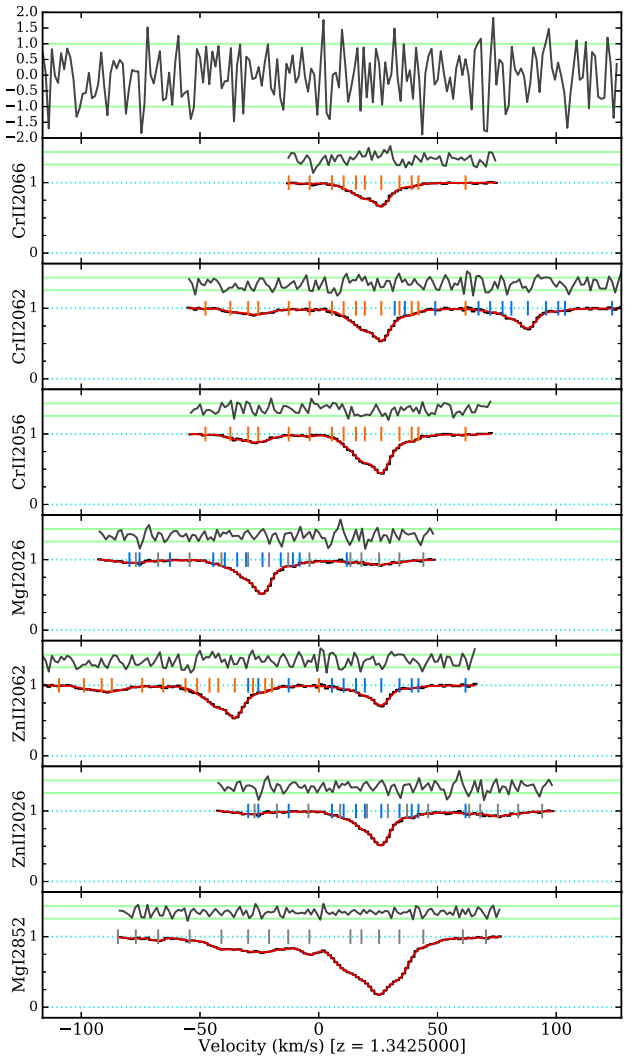

Figure 8. Same as Fig. 2 but for the Keck/HIRES spectrum of the $z_{\rm abs} = 1.342$ absorber towards J0841+0312.

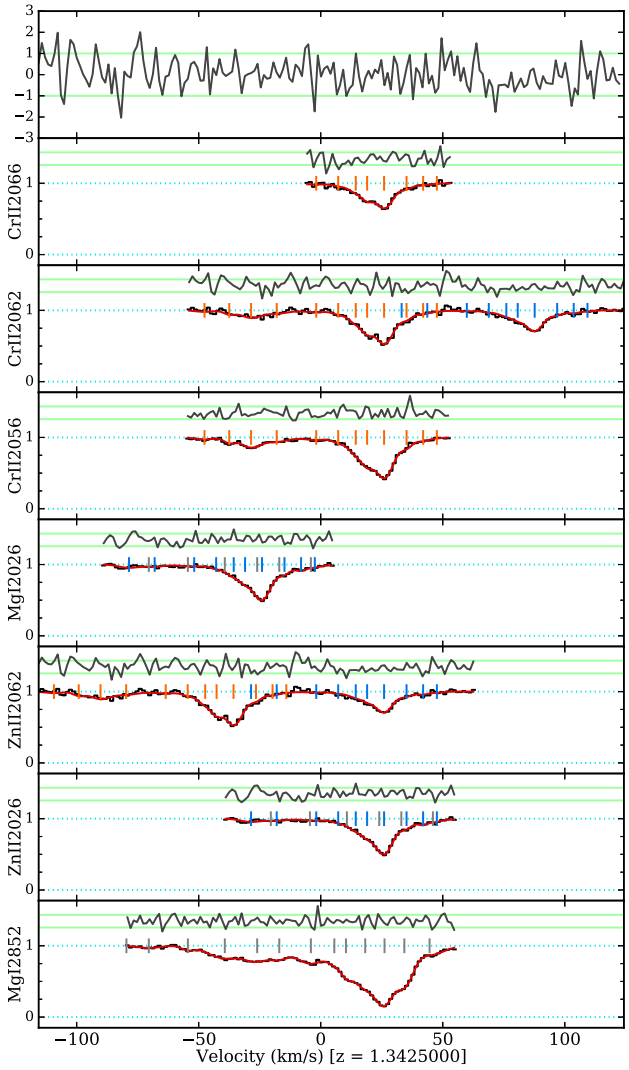

Figure 9. Same as Fig. 8 but for the VLT/UVES spectrum of the $z_{\rm abs} = 1.342$ absorber towards J0841+0312.

below our threshold of 1.2, so this absorber is accepted into our main results.

As mentioned in Section 2.2, the spectrum of Q1755+57 is the only one in which the Zn and Cr II transitions are not all covered by the same exposures. Of the 13 exposures contributing to the HIRES spectrum, 4 used the 318–605-nm wavelength setting which covers the *Zn* II λ2026 transition but not the redder Zn II transition or the Cr II triplet. It is therefore possible that residual slit positioning effects may introduce a small, spurious shift between *Zn* II λ2026 and the other transitions. However, by constructing a sub-spectrum of Q1755+57 using only the nine exposures in Table 1 that cover all the Zn and Cr II transitions, we find a $\Delta\alpha/\alpha$ value that differs by <0.4 ppm from the fiducial one in this absorber, which is <10 per cent of the statistical uncertainty. The uncertainty is just 5 per cent larger. These results indicate that any shift introduced between *Zn* II λ2026 and the other transitions by the 318–605-nm exposures causes a negligible systematic error in $\Delta\alpha/\alpha$. We therefore do not add this into the systematic error budget for this absorber in Table 2.

3.2.9 $z_{\rm abs} = 1.921$ towards Q2206−1958

This absorption system was one of the first to be studied in detailed with Keck/HIRES (e.g. Prochaska & Wolfe 1997) and is well-known to have prominent Zn and Cr II lines. Nevertheless, they are the weakest in our sample; this absorber was included in this study because the background quasar is comparatively bright ($V \sim 17.3$ mag) and a large number of archival VLT/UVES exposures are available (total exposure time, ∼15 h), providing a very high S/N of 97 pix^{-1} (see Table 1) and, therefore, a small statistical uncertainty on $\Delta\alpha/\alpha$.

The VLT/UVES spectrum in Fig. 13 shows that the Zn and Cr II absorption spans 160 km s^{-1} with two main spectral features at −50 and 10 km s^{-1}. The former is dominated by a single velocity component and provides the strongest constraint on $\Delta\alpha/\alpha$, while the latter is more complex, comprising several components. Therefore, the blend from *Mg* I λ2026 in *Zn* II λ2026 does not strongly affect the part of the absorber most important for measuring $\Delta\alpha/\alpha$. In any case, the Mg I velocity structure is strongly constrained by the *Mg* I λ2852 absorption. The residuals for individual transitions and the CRS in Fig. 13 show no evidence of data artefacts or unfitted

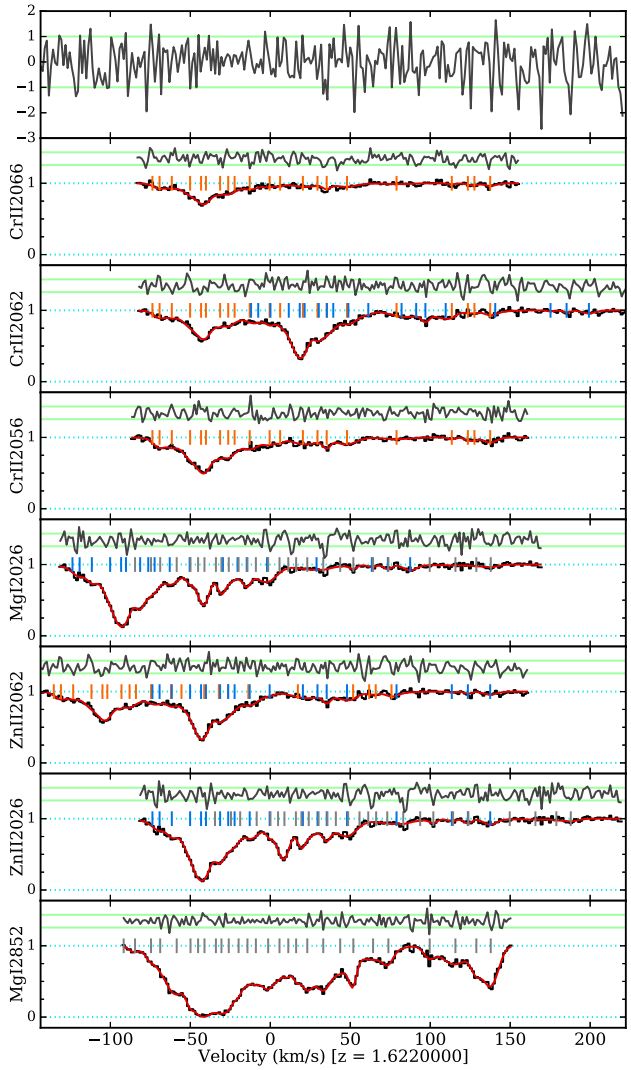

Figure 10. Same as Fig. 2 but for the Keck/HIRES spectrum of the $z_{\rm abs} = 1.622$ absorber towards J1029+1039.

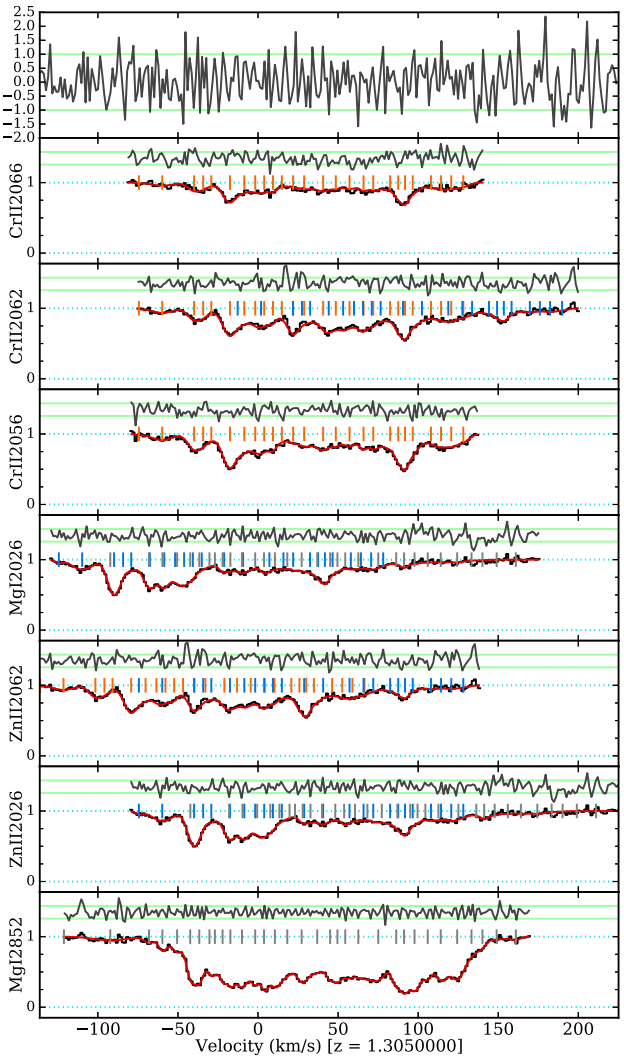

Figure 11. Same as Fig. 2 but for the Keck/HIRES spectrum of the $z_{\rm abs} = 1.305$ absorber towards J1237+0106.

structure, and the final χ^2_ν value in Table 2 is 1.06, thereby satisfying our selection criteria. This absorber is therefore accepted into our main results.

4 RESULTS

4.1 $\Delta\alpha/\alpha$ measurements and statistical uncertainties

Table 2 shows the best-fitting values of $\Delta\alpha/\alpha$, their 1σ statistical uncertainties and the final χ^2_ν resulting from the χ^2-minimization analyses of the 12 profile fits in Figs 2–13. As discussed in Section 3.2, all but one (from the VLT/UVES spectrum of J0058+0041) of the 12 fits pass our selection criteria for ensuring reliable $\Delta\alpha/\alpha$ measurements. We therefore only consider the other 11 $\Delta\alpha/\alpha$ measurements in the remaining analysis. However, none of our conclusions would change if the one rejected measurement was included. The $|\Delta\alpha/\alpha|$ values in Table 2 for these 11 measurements are all <5.5 ppm, with an average statistical uncertainty of 6.6 ppm. The uncertainties range between 2.7 and 12.9 ppm. Two absorbers have uncertainties <3 ppm, which is comparable with recent, high-precision measurements of individual systems which utilize all transitions, not just Zn and Cr II (e.g. Molaro et al. 2013; Evans et al. 2014).

Using only the statistical errors in Table 2, the weighted mean $\Delta\alpha/\alpha$ is $\langle\Delta\alpha/\alpha\rangle_{\rm w} = 0.30 \pm 1.44$ ppm, which is clearly consistent with no cosmological variation in α. Note that this precision is similar to that of the large absorber samples from Keck and VLT (≈1.2 ppm; Webb et al. 2001; Murphy et al. 2004; Webb et al. 2011; King et al. 2012) and somewhat better than that of the 23-absorber VLT sample of Chand et al. (2004) reanalysed by Wilczynska et al. (2015), ≈2.3 ppm. However, the uncertainties quoted for these previous studies were not just statistical and included some systematic effects. The χ^2 of the $\Delta\alpha/\alpha$ values around our weighted mean – again, considering only statistical errors – is 0.72 per degree of freedom, with an associated probability (that χ^2 should be larger by random chance alone) of 71 per cent. Assuming that $\Delta\alpha/\alpha$ does not vary significantly between absorbers, this indicates that additional, systematic errors that have random magnitude and sign in individual absorbers, are unlikely to be as large or larger than the statistical errors. If they were, we should observe a larger scatter in

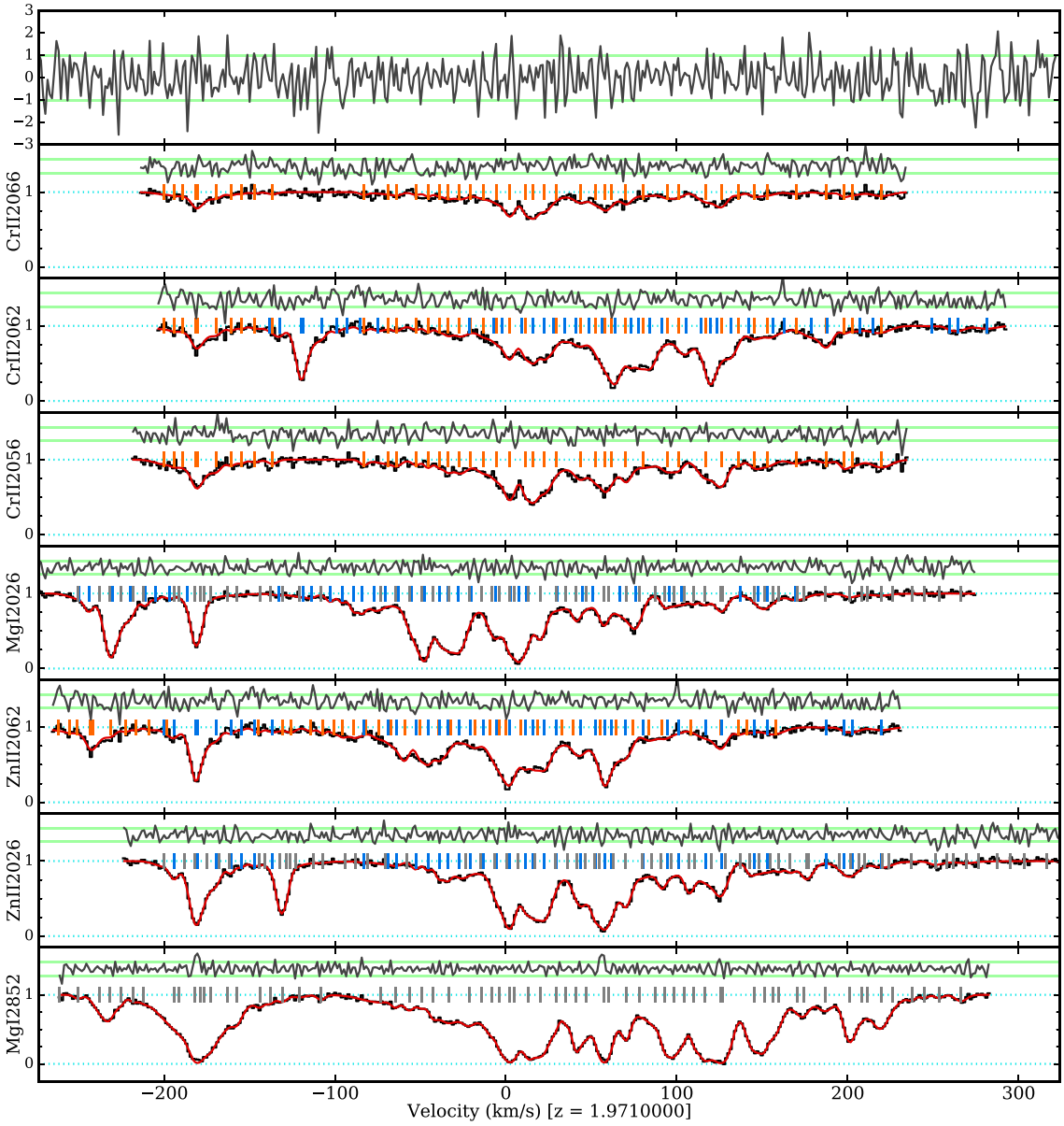

Figure 12. Same as Fig. 2 but for the Keck/HIRES spectrum of the $z_{\rm abs} = 1.971$ absorber towards Q1755+57.

$\Delta\alpha/\alpha$ than expected from the statistical errors alone, and a larger χ^2 value. Nevertheless, we consider and quantify the most important sources of systematic errors in the next Section below before further analysing the $\Delta\alpha/\alpha$ sample in Section 4.3.

4.2 Systematic uncertainties

4.2.1 Long-range distortions

The main advantage of using only the Zn and Cr II transitions to measure $\Delta\alpha/\alpha$ is that they are very sensitive to α variation while, by virtue of their wavelength proximity, insensitive to long-range distortions of the wavelength scale. Indeed, as discussed in Section 1, a distortion of 0.2 m s^{-1} Å^{-1}, which is typical of those found in recent studies, would only cause a spurious shift of 16 m s^{-1} between the *Zn* II λ2026 and *Cr* II λ2062 transitions, and equation (1) implies that this would cause a systematic error in $\Delta\alpha/\alpha$ of only 0.3 ppm per absorber. However, this simple estimate will be conservative because *Zn* II λ2026 is bluewards of all three Cr II transitions, while *Zn* II λ2062 is redwards of two and bluewards of the other. This more complicated pattern will decrease the systematic error in $\Delta\alpha/\alpha$ for a given, assumed distortion. For the four absorbers in Table 2 with the smallest statistical errors in $\Delta\alpha/\alpha$, we tested the effect of introducing a 0.2 m s^{-1} Å^{-1} distortion into each exposure, recombining these distorted exposures in UVES_POPLER, and minimizing χ^2 again using the final profile models. The effect is 0.15–0.25 ppm, smaller than the 0.3 ppm expected from the simple estimate above. In previous studies where all transitions were used in the MM analysis, long-range distortions of this magnitude were found to cause systematic errors in $\Delta\alpha/\alpha$ of ∼5–10 ppm (e.g. Evans et al. 2014). This demonstrates the resistance to long-range distortions of the Zn/Cr II approach.

Below we find that other systematic errors in our analysis are almost an order of magnitude larger than those estimated from

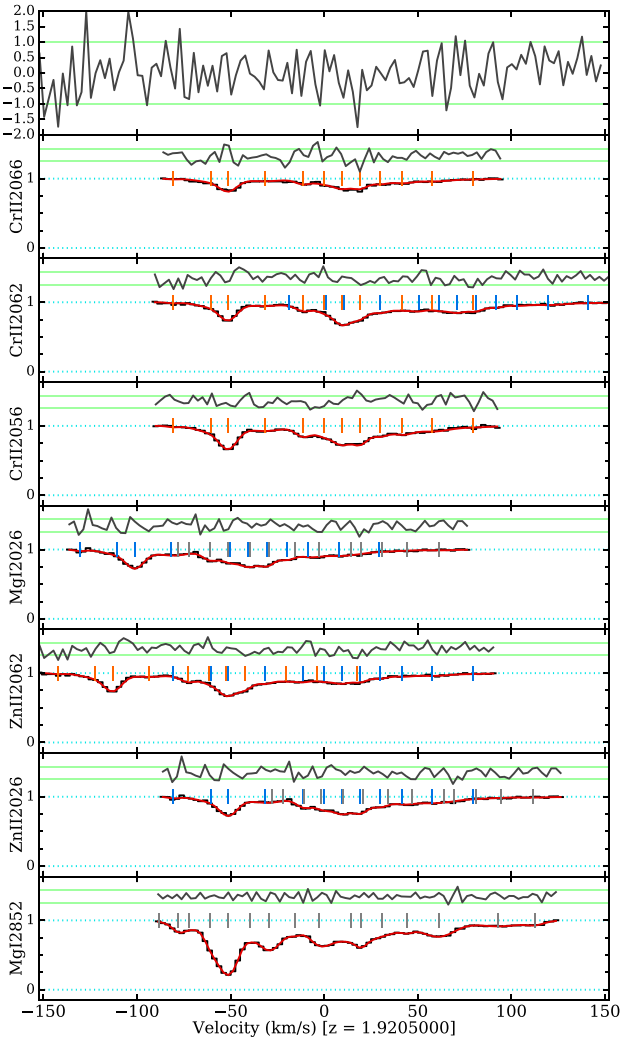

Figure 13. Same as Fig. 2 but for the VLT/UVES spectrum of the $z_{\rm abs} = 1.921$ absorber towards Q2206−1958.

long-range distortions above. We therefore ascribe the simple, possibly conservative estimate of 0.3 ppm to the systematic error budget of each absorber from this effect. This is reflected in Table 2. When deriving a weighted mean $\Delta\alpha/\alpha$ for all absorbers (Section 4.3 below), we further assume that the magnitude and sign of the long-range distortions may be treated as random from spectrum to spectrum. figs 5 and 8 of Whitmore & Murphy (2015) indeed show significant variation, but the variation is complex and not understood, so we expect this assumption to be only partially true. Nevertheless, that this systematic error is relatively small in our Zn/Cr II analysis means that neglecting this complication will have a negligible effect on the overall systematic error budget.

4.2.2 *Intra-order distortions*

While the proximity of the Zn and Cr II transitions to each other makes their exclusive use insensitive to long-range distortions, it does leave this approach vulnerable to short-range, intra-order distortions. The Cr II triplet and *Zn* II λ2062 typically span only half the free spectral range of a HIRES or UVES echelle order, while *Zn* II λ2026 typically falls one or two echelle orders bluewards of these. Therefore, for a single absorption system, the magnitude of the velocity shifts generated between these transitions, and so the systematic effect on $\Delta\alpha/\alpha$, clearly depends on the amplitude of the distortion, the shape of the distortion pattern repeated from order to order, and where the Zn and Cr II transitions fall within their respective orders. The effect on $\Delta\alpha/\alpha$ will be random in sign and magnitude for different absorbers, so it will tend to average to zero for a large sample. However, for a modest sample of 11 measurements, the effect is important to assess.

Our approach to testing the sensitivity of $\Delta\alpha/\alpha$ to this effect is to apply a 'saw-tooth' velocity distortion to each echelle order's wavelength scale, for all exposures of every quasar in our sample. That is, a velocity shift of $\Delta v = 200\ {\rm m\,s^{-1}}$ is applied to the centre of each order, falling away linearly to $-\Delta v$ at the order edges. Once the distorted orders are recombined with UVES_POPLER, $\Delta\alpha/\alpha$ is re-measured in each absorber using its final profile model as a starting point for the χ^2 minimization procedure. A similar approach was used in several other recent varying-constant studies (e.g. Malec et al. 2010; Molaro et al. 2013; Bagdonaite et al. 2014; Evans et al. 2014), with the latter three using smaller amplitudes of $\Delta v = 100\ {\rm m\,s^{-1}}$ which are typical of those found in both HIRES and UVES spectra in recent studies (Whitmore et al. 2010; Whitmore & Murphy 2015). However, because this is the largest systematic effect for our study, we use a larger amplitude to ensure it includes most, if not all potential distortions in the quasar spectra.

We find that the mean deviation in $\Delta\alpha/\alpha$ caused by introducing the 'saw-tooth' intra-order distortions is 2.03 ppm and, as expected, the magnitude and sign varies randomly from absorber to absorber. Given that we do not know the true shape of the intra-order distortion pattern or its amplitude for any individual absorber, we ascribe this mean value to the systematic error budget for each absorber. This is reflected in Table 2.

4.2.3 *Spectral redispersion*

The exposures of each quasar were redispersed on to a common log-linear wavelength grid, a process that slightly distorts the absorption line shapes and introduces small correlations in the flux and flux uncertainties of neighbouring pixels. That is, the redispersion process will cause small, spurious velocity shifts between the absorption profiles of different transitions, and hence a systematic error in $\Delta\alpha/\alpha$ that varies in sign and magnitude from absorber to absorber.

As in other recent works (e.g. Malec et al. 2010; van Weerdenburg et al. 2011; Molaro et al. 2013; Evans et al. 2014), we quantify this effect by slightly altering the dispersion of the final wavelength grid, by ±0.01 and $\pm0.02\ {\rm km\,s^{-1}}$, for each quasar and re-measuring $\Delta\alpha/\alpha$ of each absorber using its final profile model for the χ^2 minimization. The mean deviation of these four measurements from the fiducial $\Delta\alpha/\alpha$ value indicates the systematic uncertainty for each absorber, i, $\sigma^i_{\rm disp}$. However, with only four measurements, this approach will underestimate the effect for some absorbers (and overestimate it for others). To address this, we first noted an expected correlation between $\sigma_{\rm disp}$ and the statistical uncertainty on $\Delta\alpha/\alpha$, $\sigma_{\rm stat}$. A linear least-squares fit yields the relationship $\sigma_{\rm disp}[{\rm ppm}] \approx 0.15 + 0.12 \times \sigma_{\rm stat}[{\rm ppm}]$. Therefore, for absorber i, we assigned the larger of the original estimate, $\sigma^i_{\rm disp}$, and the value derived from this relationship, as the systematic error from redispersion for that absorber.

Table 2 shows the total systematic error budget for each absorber. As discussed in Sections 4.2.1 and 4.2.2 above, the systematic uncertainty from long-range and intra-order distortions are taken to be

the same for all absorbers, 0.3 and 2.03 ppm, respectively. Only the systematic uncertainty from redispersion effects vary from absorber to absorber, so for simplicity we only present the quadrature sum of all systematic errors in Table 2.

4.2.4 *Isotopic abundance variations*

The profile fits to the Zn II, Cr II, and Mg I absorption lines included the measured or calculated isotopic and hyperfine structures reviewed recently in Murphy & Berengut (2014) and the terrestrial relative isotopic abundances (Rosman & Taylor 1998). However, if the relative isotopic abundances of Zn and/or Cr are different in the absorption clouds, this will shift the velocity centroids of the absorption features, causing systematic errors in $\Delta\alpha/\alpha$ measured from our fits which use the terrestrial abundances. This is a well-recognized problem (e.g Murphy et al. 2001a,b), especially for fits involving Mg I/II transitions because the separations between isotopic components are relatively large (because Mg is a relatively light atom). Indeed, Fenner, Murphy & Gibson (2005) found that if the heavy isotopes of Mg ($^{25,\,26}$Mg; total relative terrestrial abundance of 21 per cent) were completely absent in quasar absorption clouds, a systematic error in $\Delta\alpha/\alpha$ of $\approx$4.5 ppm would be induced in a MM analysis of the strong Mg I/II and Fe II transitions.

However, the Zn/Cr II combination is more resistant to this systematic error, mainly because of the smaller isotopic shifts in these heavier atoms. The Mg I transitions are also decoupled from $\Delta\alpha/\alpha$ in our fits (see Section 3.1), so variations in the Mg isotopic abundances will not affect our results. Using a chemical evolution model for spiral galaxies like our Milky Way, Fenner et al. (2005) predicted that the isotopes of Cr and Zn with the lowest terrestrial abundances will be less abundant in gas with low metallicities typical of most quasar absorbers. And while our absorbers will have higher-than-average metallicities – they were selected because of their very strong metal absorption – and this may reduce the effect on $\Delta\alpha/\alpha$, we cannot rule out this systematic effect on such grounds.

If we make the extreme assumption that the sub-dominant isotopes are absent in the absorbers, our fits will find centroids for the Zn II and Cr II transitions that are too red by $\approx$100 m s^{-1} and too blue by $\approx$10 m s^{-1}, respectively. Considering just the *Zn* II λ2026 and *Cr* II λ2056 transitions, this would cause a systematic error in $\Delta\alpha/\alpha$ of -2.3 ppm (cf. 4.5 ppm for the Mg I/II and Fe II combination). Just as for the long-range distortions (Section 4.2.1), this effect will be diminished by *Zn* II λ2062 falling amongst the Cr II triplet. Indeed, in our best-constrained absorber, that towards J0108$-$0037, we find that $\Delta\alpha/\alpha$ shifts by -2.1 ppm if we remove the sub-dominant isotopes from the fit. This is only marginally larger than our total error budget of 1.7 ppm for the ensemble of 11 measurements; correcting for even this extreme possibility would place our measured $\Delta\alpha/\alpha$ value just 1.5σ above zero.

Given that $\Delta\alpha/\alpha$ is relatively insensitive to this effect, our general lack of information about the isotopic abundances in the absorbers, and following all previous measurements which include the more sensitive Mg I/II transitions, we do not attempt to formally include this effect in our systematic error budget. However, our main conclusions in Section 6 are explicitly stated with the assumption of terrestrial isotopic abundances.

4.3 Statistical analysis of main results

Table 2 shows the best-fitting value of $\Delta\alpha/\alpha$, the 1σ statistical uncertainty, and systematic uncertainty for all absorbers in our study.

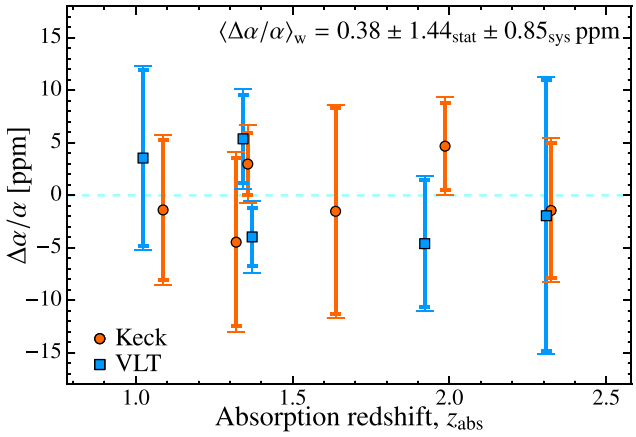

Figure 14. The $\Delta\alpha/\alpha$ measurements for the 11 profile fits that pass our selection criteria (i.e. all but the VLT spectra of J0058+0041 from Table 2) versus their absorption redshifts, $z_{\rm abs}$. The thicker, shorter error bars represent the 1σ statistical uncertainties and the thinner, longer ones represent the quadrature sum of the statistical and systematic uncertainties (see Table 2). The values derived from Keck spectra are shown as circles, and values from VLT as squares. Note that the Keck results are all shifted by $\Delta z = 0.015$ for clarity. The weighted mean $\Delta\alpha/\alpha$ from the 11 measurements, $\langle\Delta\alpha/\alpha\rangle_{\rm w}$ (equation 2), is also shown. These results were derived using the terrestrial isotopic abundances for Zn and Cr; see discussion of this potential systematic error in Section 4.2.4.

Note that, as described in Section 3.2.1, the result from the VLT spectrum of J0058+0041 (italics in Table 2) is not considered further in our analysis because the fit in that case returned a χ^2_ν value exceeding our threshold value of 1.2. The remaining 11 $\Delta\alpha/\alpha$ values and uncertainties are plotted in Fig. 14 against absorption redshift and delineated by telescope. It is immediately clear that all 11 values are consistent with no variation in α and that there is no systematic offset from $\Delta\alpha/\alpha = 0$. There is no significant trend with redshift, in either the sample as a whole or from either telescope separately. All 11 results are also consistent with each other. In particular, a reliable $\Delta\alpha/\alpha$ measurement was made with both Keck and VLT spectra of the same two absorbers towards PHL957 and J0841+0312, and these are found to be consistent with each other.

As discussed in Sections 4.2.2 and 4.2.3, the two largest systematic effects on $\Delta\alpha/\alpha$ – those from intra-order distortions and spectral redispersion – are random from absorber to absorber. Therefore, we combined the results to form a weighted mean in a straightforward way: the weight for each absorber, i, is the inverse sum of the statistical and systematic variances, i.e. $w_i \equiv (\sigma^2_{i,\rm stat} + \sigma^2_{i,\rm sys})^{-1}$; the statistical uncertainty is $\sigma_{\rm stat} = 1/\sqrt{\sum_i 1/(\sigma_{i,\rm stat})^2}$; and the systematic uncertainty is the quadrature difference between $\sigma_{\rm tot} = 1/\sqrt{\sum_i w_i}$ and $\sigma_{\rm stat}$. This provides our main result: the weighted mean $\Delta\alpha/\alpha$ from the 11 measurements, with 1σ statistical and systematic uncertainties:

$$\langle\Delta\alpha/\alpha\rangle_{\rm w} = 0.38 \pm 1.44_{\rm stat} \pm 0.85_{\rm sys}\ \text{ppm}\,. \qquad (2)$$

The scatter around this weighted mean is consistent with expectations from the individual error bars: $\chi^2 = 5.29$ which, for 10 degrees of freedom, has an associated probability (of being exceeded by chance alone) of 87 per cent. The weighted means for the Keck and VLT sub-samples are $1.6 \pm 2.0_{\rm stat} \pm 1.1_{\rm sys}$ (six absorbers) and $-1.0 \pm 2.1_{\rm stat} \pm 1.3_{\rm sys}$ ppm (five absorbers), respectively; these are consistent with each other within $0.8\sigma_{\rm comb}$ where $\sigma_{\rm comb}$ is the quadrature sum of the statistical and systematic uncertainties. The scatter amongst the VLT measurements is consistent with the

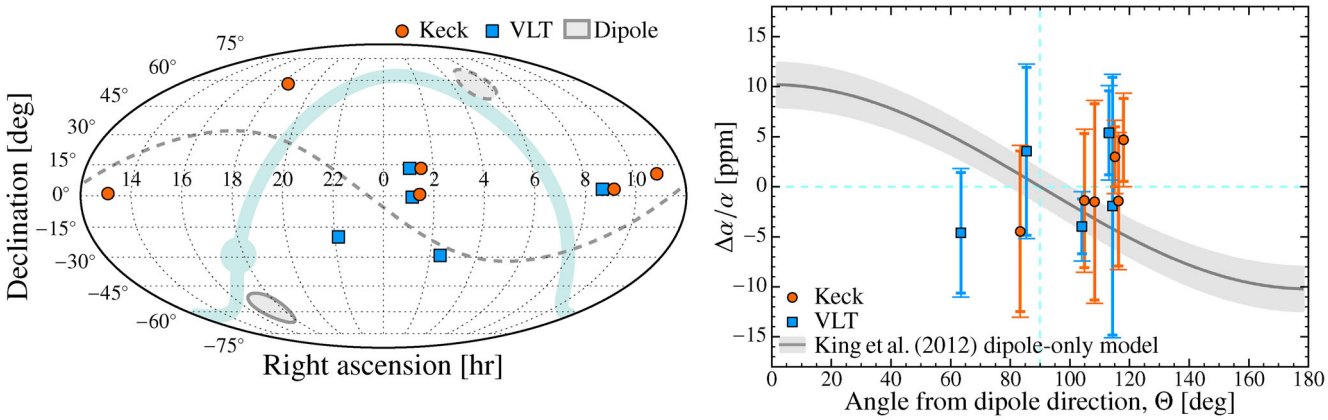

Figure 15. Left-hand panel: angular distribution of our nine quasar lines of sight across the sky. The quasars observed with Keck are shifted by ΔRA = 0.5 h for clarity. The shaded ellipse with the solid line represents the 1σ uncertainty in the position of the pole in the dipole-only model of $\Delta\alpha/\alpha$ from King et al. (2012); the ellipse with the dashed line represents the anti-pole and the dashed curve is the dipole's equator. The lighter blue shading represents the Galactic plane, with the bulge indicating the Galactic Centre. Right-hand panel: Comparison of our 11 new Zn/Cr II measurements of $\Delta\alpha/\alpha$ with the dipole expectation (solid line; shading indicates the $\pm1\sigma$ uncertainty). Our quasar sight-lines are distributed near the equator of the dipole model, where $\Delta\alpha/\alpha$ is predicted to be <5 ppm, so we cannot rule out or confirm the dipole with our new measurements alone.

uncertainties ($\chi^2 = 3.1$ around the VLT weighted mean, with associated probability of 53 per cent). The scatter amongst the six Keck results may seem too small, relative to the uncertainties, in Fig. 14: $\chi^2 = 1.5$ around the Keck weighted mean. However, for such a small sample, this is expected to occur 9 per cent of the time by chance alone, so there is no strong evidence for an underestimated scatter (or overestimated uncertainties).

5 DISCUSSION

Our new measurement of $\Delta\alpha/\alpha$ in equation (2) is the first from a statistical sample of absorbers that is resistant to long-range distortions at the <1 ppm level. $\Delta\alpha/\alpha$ has been measured in just four other distinct absorbers with distortion-corrected spectra, by Evans et al. (2014) and very recently by Kotuš et al. (2016), using MM analyses of a large variety of transitions. Evans et al. (2014) studied three absorbers towards a single quasar (HS1549+1919; $z_{\rm abs}$ = 1.143, 1.342 and 1.802) using three different telescopes (Keck, Subaru and VLT). The weighted mean from their nine measurements is $\langle\Delta\alpha/\alpha\rangle_{\rm w} = -5.4 \pm 3.3_{\rm stat} \pm 1.5_{\rm sys}$ ppm. Kotuš et al. (2016) analysed the very complex $z_{\rm abs} = 1.1508$ absorber towards HE0515−4414 (the brightest known southern quasar at $z_{\rm em} > 1$) using very high-quality VLT/UVES spectra (S/N ∼ 250 per 1.3-km s^{-1} pixel). They obtained the most precise measurement in a single absorber to date: $\Delta\alpha/\alpha = -1.4 \pm 0.6_{\rm stat} \pm 0.6_{\rm sys}$ ppm. These two distortion-corrected results are consistent with each other and with our new distortion-resistant measurement, and the combined constraint on $\Delta\alpha/\alpha$ is a weighted mean (derived with the same approach as equation 2) of

$$\langle\Delta\alpha/\alpha\rangle_{\rm w} = -1.2 \pm 0.5_{\rm stat} \pm 0.5_{\rm sys}\ {\rm ppm}\,. \quad (3)$$

This is the best current limit on variations in α using quasar absorption systems, assuming that it does not vary across the sky.

Given that the quasars in our sample have a reasonable distribution across the sky, testing whether α displays such spatial variation is possible, in principle. However, the sample is still relatively small (nine quasars) so, instead, a comparison with recent, possible evidence for such variations is more instructive. Prior to long-range distortions being found in UVES and HIRES spectra, the large statistical Keck and VLT samples were combined to search for angular variations in $\Delta\alpha/\alpha$ (Webb et al. 2011; King et al. 2012). The simplest model of such variations, a dipole, was found to be required at ≈4σ significance, with the pole in the direction (RA, Dec.) = (17.4 ± 0.9 h, −58 ± 9°) and deviating by $\Delta\alpha/\alpha = 10.2^{+2.2}_{-1.9}\cos(\Theta)$ ppm with the angular separation, Θ, from this direction (King et al. 2012). Whitmore & Murphy (2015) found that long-range distortions likely explain the VLT results and, at least partially, the Keck results that provide a basis for this dipole result. Nevertheless, new measurements that are resistant to, or corrected for, the long-range distortions can in principle be used to rule out or confirm this variation in α across the sky.

The left-hand panel of Fig. 15 compares the distribution of our quasar sight-lines on the sky with the position of the putative dipole, and the right-hand panel compares our new $\Delta\alpha/\alpha$ measurements with the predicted value from the dipole model. It is immediately clear that our quasar sight-lines are positioned around the equator of the dipole model, with angular separations clustered near Θ ≈ 90° where the model predicts $\Delta\alpha/\alpha < 5$ ppm. This precludes an effective test of the dipole model using our new Zn/Cr II measurements. Indeed, the χ^2 between our values and the model is 14.4 which, for 11 degrees of freedom, has an associated probability of 21 per cent, i.e. the data are consistent with the model. The distortion-corrected measurements from HE0515−4414 (Kotuš et al. 2016) and HS1549+1919 (Evans et al. 2014) have Θ values of 78° and 80°, respectively, so adding them to this comparison would not provide significant additional discriminating power. The simplest approach to rule out or confirm the dipole model would be to obtain a modest sample of distortion-correct spectra and/or strong Zn/Cr II absorbers, towards quasars within ∼20° of the pole and/or anti-pole.

Our new measurements demonstrate the important advantages of using only the Zn and Cr II transitions to measure $\Delta\alpha/\alpha$, primarily their high sensitivity to α-variation and resistance to long-range distortions in the wavelength calibration of the quasar spectra. However, there are some disadvantages of this approach. First, there are only two strong Zn II transitions and three strong Cr II transitions, so each $\Delta\alpha/\alpha$ measurement relies on fewer transitions than is typical for most MM analyses, which reduces the statistical precision available. Secondly, they are normally weak in most absorption systems, so large samples of high-resolution quasar spectra are needed before a statistical sample of strong-enough Zn/Cr II absorbers can be

identified towards bright-enough quasars. Pre-selection of targets could be made efficiently from short, moderate-resolution ($R \sim 10\,000$) follow-up spectra of absorbers which show possible Zn and Cr II absorption in low-resolution spectra from large surveys (e.g. from the Sloan Digital Sky Survey). Thirdly, the blends between the $Mg\,\textsc{i}\,\lambda2026$ and $Zn\,\textsc{ii}\,\lambda2026$ transitions, and to some extent the fact that $Cr\,\textsc{ii}\,\lambda2062$ and $Zn\,\textsc{ii}\,\lambda2062$ overlap in absorbers with extended velocity structure, complicates the analysis. We have demonstrated here how that can be overcome by using $Mg\,\textsc{i}\,\lambda2852$ to constrain the $Mg\,\textsc{i}\,\lambda2026$ blend, with the two transitions 'decoupled' in the fitting procedure (see Section 3.1). Despite these disadvantages, we have demonstrated that Zn/Cr II measurements of $\Delta\alpha/\alpha$ offer an important complement to other MM analyses: the latter may, in principle, achieve higher statistical precision but they are more vulnerable to long-range instrumental systematic effects than the Zn/Cr II approach.

6 CONCLUSIONS

Comparing the two Zn II and the three Cr II transitions falling in the narrow rest wavelength range of 2026–2066 Å is, in principle, the most sensitive to α-variation of all metal line combinations used in many-multiplet studies to date (Fig. 1). However, these transitions are rarely strong enough, even in damped Lyman α systems, to be very useful in constraining $\Delta\alpha/\alpha$. We identified nine absorption systems at $z_{\rm abs} = 1.0$–2.4 with strong Zn/Cr II absorption towards nine relatively bright quasars ($r = 16.1$–18.3 mag) and obtained new and/or archival spectra with Keck/HIRES (6 quasars) and VLT/UVES (6 quasars, three in common with Keck) with high S/N (mean 54 pix^{-1} around Zn/Cr II). The quasar spectra and Zn/Cr II absorption profile fits are publicly available in Murphy et al. (2016). Of the 12 profile fits (Figs 2–13), 11 passed our stringent selection criteria to provide robust new measurements of $\Delta\alpha/\alpha$. These all lie within 5.5 ppm of zero, with total (quadrature addition of statistical and systematic) uncertainties of 3.5–13.2 ppm, and all formally consistent with $\Delta\alpha/\alpha = 0$. There is no evidence of redshift evolution in $\Delta\alpha/\alpha$ or any systematic difference between the Keck and VLT measurements. The final weighted mean $\Delta\alpha/\alpha$ from all 11 measurements, with 1σ statistical and systematic uncertainties, is $0.4 \pm 1.4_{\rm stat} \pm 0.9_{\rm sys}$ ppm (1σ, equation 2), consistent with no variation in α. As with other many-multiplet measurements of $\Delta\alpha/\alpha$, this assumes that the relative isotopic abundances of Zn and Cr in the absorbers are similar to the terrestrial values. Assuming that isotopes with the lowest terrestrial abundances are completely absent in the absorbers, $\Delta\alpha/\alpha$ would be corrected to 2.5 ± 1.7 ppm, still consistent with no variation in α.

An important advantage of the Zn/Cr II approach demonstrated here is its resistance to long-range distortions in the wavelength calibration of the quasar spectra. Such systematic effects will have significantly impacted all previous $\Delta\alpha/\alpha$ measurements with the many-multiplet method, except for the recent analyses of distortion-correct spectra by Evans et al. (2014) and Kotuš et al. (2016). Indeed, these distortions likely explain previous evidence for α-variation from large Keck and VLT absorber samples (Whitmore & Murphy 2015). However, the wavelength proximity of the Zn and Cr II transitions, and their high sensitivity to α-variation, mean that long-range distortions only cause a $\sim$0.3 ppm systematic error in each absorber. The largest systematic error in our Zn/Cr II measurements – $\sim$2.0 ppm for each absorber – stems, instead, from intra-order distortions. Errors from the redispersion of the quasar spectra (necessary when combining many exposures of a single quasar together) cause errors of 0.5–2.3 ppm in each absorber, evidently scaling with its statistical uncertainty.

Our new measurements are consistent with the only distortion-corrected measurements so far, with a total ensemble uncertainty (1.7 ppm; quadrature sum of final statistical and systematic uncertainties) approximately half that from the nine measurements by Evans et al. (2014, 3.6 ppm) and almost twice that obtained from the single, very high-S/N absorber of Kotuš et al. (2016, 0.9 ppm). Combined, these measurements provide the best current restriction on variations in α, with a weighted mean $\Delta\alpha/\alpha = -1.2 \pm 0.5_{\rm stat} \pm 0.5_{\rm sys}$ (1σ, equation 3) at redshifts $z_{\rm abs} = 1.0$–2.4. Despite this precision, the spatial distribution of the quasars precludes a rigorous test of the dipole-like variation in α across the sky from the large Keck and VLT samples in King et al. (2012) (i.e. taking evidence for that at face value, ignoring the concerns about long-range distortions raised above). New $\Delta\alpha/\alpha$ measurements at a wider variety of sky coordinates, using distortion-corrected spectra and/or the Zn/Cr II approach, would enable such a test.

ACKNOWLEDGEMENTS

We thank Sebastian Lopez for initial discussions about using Zn and Cr II to measure $\Delta\alpha/\alpha$, and Julija Bagdonaite and Jonathan Whitmore for assistance with Fig. 15. MTM thanks the Australian Research Council for *Discovery Projects* grant DP110100866 which supported this work. Some of the data presented herein were obtained at the W.M. Keck Observatory, which is operated as a scientific partnership among the California Institute of Technology, the University of California and the National Aeronautics and Space Administration. The Observatory was made possible by the generous financial support of the W.M. Keck Foundation. We wish to recognize and acknowledge the very significant cultural role and reverence that the summit of Maunakea has always had within the indigenous Hawaiian community. We are most fortunate to have the opportunity to conduct observations from this mountain. Other data presented herein were based on observations made with ESO Telescopes at the La Silla Paranal Observatory under programme IDs 65.O-0158, 67.A-0022, 072.A-0346, 074.A-0201, 079.A-0600, 082.A-0682, 082.A-0569, 083.A-0874 and 084.A-0136.

REFERENCES

Agafonova I. I., Molaro P., Levshakov S. A., Hou J. L., 2011, A&A, 529, 28
Akaike H., 1974, IEEE Trans. Autom. Control, 19, 716
Bagdonaite J., Ubachs W., Murphy M. T., Whitmore J. B., 2014, ApJ, 782, 10
Bahcall J. N., Sargent W. L. W., Schmidt M., 1967, ApJ, 149, L11
Berengut J. C., 2011, Phys. Rev. A, 84, 052520
Berengut J. C., Dzuba V. A., Flambaum V. V., 2003, Phys. Rev. A, 68, 022502
Campbell P., Billowes J., Grant I. S., 1997, J. Phys. B: Atomic, 30, 2351
Carswell R. F., Webb J. K., 2014, Astrophysics Source Code Library, record ascl:1408.015
Chand H., Srianand R., Petitjean P., Aracil B., 2004, A&A, 417, 853
Cowie L. L., Songaila A., 1995, ApJ, 453, 596
Dekker H., D'Odorico S., Kaufer A., Delabre B., Kotzlowski H., 2000, Proc. SPIE, 4008, 534
Dixit G., Nataraj H. S., Sahoo B. K., Chaudhuri R. K., Majumder S., 2008, Jo. Phys. B: Atomic, 41, 025001
Dzuba V. A., Flambaum V. V., Webb J. K., 1999, Phys. Rev. Lett., 82, 888
Evans T. M. et al., 2014, MNRAS, 445, 128
Fenner Y., Murphy M. T., Gibson B. K., 2005, MNRAS, 358, 468

Griest K., Whitmore J. B., Wolfe A. M., Prochaska J. X., Howk J. C., Marcy G. W., 2010, ApJ, 708, 158
Hannemann S., Salumbides E. J., Witte S., Zinkstok R. T., van Duijn E.-J., Eikema K. S. E., Ubachs W., 2006, Phys. Rev. A, 74, 012505
Herbert-Fort S., Prochaska J. X., Dessauges-Zavadsky M., Ellison S. L., Howk J. C., Wolfe A. M., Prochter G. E., 2006, PASP, 118, 1077
King J. A., Webb J. K., Murphy M. T., Flambaum V. V., Carswell R. F., Bainbridge M. B., Wilczynska M. R., Koch F. E., 2012, MNRAS, 422, 3370
Kotuš S., Murphy M. T., Carswell R. F., 2016, MNRAS, in press
Levshakov S. A., Centurión M., Molaro P., D'Odorico S., 2005, A&A, 434, 827
Levshakov S. A., Molaro P., Lopez S., D'Odorico S., Centurión M., Bonifacio P., Agafonova I. I., Reimers D., 2007, A&A, 466, 1077
Malec A. L., 2016, PhD thesis, Swinburne University of Technology
Malec A. L. et al., 2010, MNRAS, 403, 1541
Matsubara K., Tanaka U., Imajo H., Urabe S., Watanabe M., 2003, App. Phys. B, 76, 209
Molaro P., Reimers D., Agafonova I. I., Levshakov S. A., 2008a, Eur. Phys. J. Spec. Top., 163, 173
Molaro P., Levshakov S. A., Monai S., Centurión M., Bonifacio P., D'Odorico S., Monaco L., 2008b, A&A, 481, 559
Molaro P. et al., 2013, A&A, 555, A68
Murphy M. T., 2016, UVES_popler: POst PipeLine Echelle Reduction software. doi:10.5281/zenodo.44765
Murphy M. T., Berengut J. C., 2014, MNRAS, 438, 388
Murphy M. T., Webb J. K., Flambaum V. V., Dzuba V. A., Churchill C. W., Prochaska J. X., Barrow J. D., Wolfe A. M., 2001a, MNRAS, 327, 1208
Murphy M. T., Webb J. K., Flambaum V. V., Churchill C. W., Prochaska J. X., 2001b, MNRAS, 327, 1223
Murphy M. T., Webb J. K., Flambaum V. V., Prochaska J. X., Wolfe A. M., 2001c, MNRAS, 327, 1237
Murphy M. T., Webb J. K., Flambaum V. V., 2003, MNRAS, 345, 609
Murphy M. T., Flambaum V. V., Webb J. K., Dzuba V., Prochaska J., Wolfe A., 2004, Lecture Notes in Physics, 648, 131
Murphy M. T., Tzanavaris P., Webb J. K., Lovis C., 2007, MNRAS, 378, 221
Murphy M. T., Webb J. K., Flambaum V. V., 2008, MNRAS, 384, 1053
Murphy M. T., Malec A. L., Prochaska J. X., 2016, Quasar Spectra and Zn/CrII Absorption Profile Fits for Limiting Fine-structure Constant Variability. doi:10.5281/zenodo.51504
Pettini M., Boksenberg A., Hunstead R. W., 1990, ApJ, 348, 48
Prochaska J. X., Wolfe A. M., 1997, ApJ, 474, 140
Quast R., Reimers D., Levshakov S. A., 2004, A&A, 415, L7
Rahmani H. et al., 2013, MNRAS, 435, 861
Rosman K. J. R., Taylor P. D. P., 1998, J. Phys. Chem. Ref. Data, 27, 1275
Salumbides E. J., Hannemann S., Eikema K. S. E., Ubachs W., 2006, MNRAS, 373, L41
Songaila A., Cowie L. L., 2014, ApJ, 793, 103
van Weerdenburg F., Murphy M. T., Malec A. L., Kaper L., Ubachs W., 2011, Phys. Rev. Lett., 106, 180802
Varshalovich D. A., Panchuk V. E., Ivanchik A. V., 1996, Astron. Lett., 22, 6
Vogt S. S. et al., 1994, Proc. SPIE, 2198, 362
Webb J. K., Flambaum V. V., Churchill C. W., Drinkwater M. J., Barrow J. D., 1999, Phys. Rev. Lett., 82, 884
Webb J. K., Murphy M. T., Flambaum V. V., Dzuba V. A., Barrow J. D., Churchill C. W., Prochaska J. X., Wolfe A. M., 2001, Phys. Rev. Lett., 87, 091301
Webb J. K., King J. A., Murphy M. T., Flambaum V. V., Carswell R. F., Bainbridge M. B., 2011, Phys. Rev. Lett., 107, 191101
Whitmore J. B., Murphy M. T., 2015, MNRAS, 447, 446
Whitmore J. B., Murphy M. T., Griest K., 2010, ApJ, 723, 89
Wilczynska M. R., Webb J. K., King J. A., Murphy M. T., Bainbridge M. B., Flambaum V. V., 2015, MNRAS, 454, 3082
Wolfe A. M., Brown R. L., Roberts M. S., 1976, Phys. Rev. Lett., 37, 179
Zych B. J., Murphy M. T., Hewett P. C., Prochaska J. X., 2009, MNRAS, 392, 1429

This paper has been typeset from a TEX/LATEX file prepared by the author.